

Large-eddy simulations of marine boundary-layer clouds associated with cold air outbreak during the ACTIVATE campaign. Part II: aerosol–meteorology–cloud interaction

XIANG-YU LI^a, HAILONG WANG^a, JINGYI CHEN^a, SATOSHI ENDO^b, SIMON KIRSCHLER^c, CHRISTIANE VOIGT^c, EWAN CROSBIE^{d,e}, LUKE D ZIEMBA^d, DAVID PAINEMAL^{d,e}, BRIAN CAIRNS^f, JOHNATHAN W HAIR^d, ANDREA F. CORRAL^g, CLAIRE ROBINSON^e, HOSSEIN DADASHAZAR^g, ARMIN SOROOSHIAN^{g,h}, GAO CHEN^d, RICHARD ANTHONY FERRARE^d, MARY M KLEB^d, HONGYU LIUⁱ, RICHARD MOORE^d, AMY JO SCARINO^{e,d}, MICHAEL A. SHOOK^d, TAYLOR J SHINGLER^d, KENNETH LEE THORNHILL^{e,d}, FLORIAN TORNOW^{f,j}, HENG XIAO^a, XUBIN ZENG^h

^a Pacific Northwest National Laboratory

^b Brookhaven National Laboratory, Upton, NY, United States

^c Institut für Physik der Atmosphäre, Deutsches Zentrum für Luft- und Raumfahrt (DLR), Oberpfaffenhofen, Germany, and Institute for Physics of the Atmosphere, Johannes Gutenberg-University Mainz, Germany

^d NASA Langley Research Center, Hampton, VA, United States

^e Science Systems and Applications, Inc. Hampton, Hampton, VA, United States

^f NASA Goddard Institute for Space Studies, New York, NY, United States

^g University of Arizona, Department of Chemical and Environmental Engineering, Tucson, AZ, United States

^h University of Arizona, Department of Hydrology and Atmospheric Sciences, Tucson, AZ, United States

ⁱ National Institute of Aerospace, Hampton, VA, United States

^j Columbia University of New York, Center for Climate Systems Research, Earth Institute, New York, NY, United States

ABSTRACT: Aerosol effects on micro-/macro-physical properties of marine stratocumulus clouds over the Western North Atlantic Ocean (WNAO) are investigated using in-situ measurements and large-eddy simulations (LES) for two cold air outbreak (CAO) cases (February 28 and March 1, 2020) during the Aerosol Cloud meTeorology Interactions oVer the western ATLantic Experiment (ACTIVATE). The LES is able to reproduce the vertical profiles of liquid water content (LWC), effective radius r_{eff} and the cloud droplet number concentration N_c from fast cloud droplet probe (FCDP) in-situ measurements for both cases. Furthermore, we show that aerosols affect cloud properties (N_c , r_{eff} , and LWC) via the prescribed bulk hygroscopicity of aerosols ($\bar{\kappa}$) and aerosol size distributions characteristics. N_c , r_{eff} , and liquid water path (LWP) are positively correlated to $\bar{\kappa}$ and aerosol number concentration (N_a) while cloud fractional cover (CFC) is insensitive to $\bar{\kappa}$ and aerosol size distributions for the two cases. The changes to aerosol size distribution (number concentration, width, and the geometrical diameter) allow us to disentangle aerosol effects on cloud properties from the meteorological effects. We also use the LES results to evaluate cloud properties from two reanalysis products, ERA5 and MERRA-2. Comparing to LES, the ERA5 reanalysis is able to capture the time evolution of LWP and total cloud coverage within the study domain during both CAO cases while MERRA-2 underestimates them.

1. Introduction

Aerosols and clouds pose the largest uncertainty in climate projection since they mediate the radiative forcing of the Earth’s atmosphere (Seinfeld et al. 2016). An increased loading of aerosols in the atmosphere reflects more incoming solar energy to space and consequentially cools the Earth system. The increased aerosol number concentration N_a in an environment with constant liquid water content (LWC) leads to cloud droplets with smaller size and larger number concentration N_c , which makes the cloud more reflective, often called the first indirect effect, a.k.a. Twomey effect (Twomey 1977). The reduced droplet sizes can also result in less precipitation and longer cloud lifetime. The latter effect is known as the second indirect effect (Albrecht 1989). Cloud radiative properties are determined by both the cloud macrophysical properties, such

as the liquid water path (LWP) and cloud fractional coverage (CFC) and by the cloud microphysical properties, such as N_c and the effective radius r_{eff} . Global mean change in radiative forcing due to anthropogenic aerosols, relative to preindustrial era (before year 1850), is roughly estimated to be between -1.6 to -0.6 W m^{-2} with a 68% confidence interval in year 2005-2015 (Bellouin et al. 2020). However, how the anthropogenic aerosols affect LWC and CFC remains unclear (Bellouin et al. 2020; McCoy et al. 2020), which is due to the fact that LWC and CFC are predominantly determined by meteorology states but also modulated by changes in N_c through precipitation (Stevens and Feingold 2009). This is the so-called aerosol-meteorology-cloud-interaction (AMCI) problem that encompasses a wide range of spatial-temporal scales from nm-sized aerosol particles to large-scale atmospheric circulations ($O(100 \text{ km})$). Global Earth system models and even cloud resolving models suffer from coarse resolu-

Corresponding author: Xiang-Yu Li, xiangyu.li@pnnl.gov

Corresponding author: Hailong Wang, hailong.wang@pnnl.gov

tions such that vital cloud macro/micro processes in marine boundary layer cannot be physically represented.

Here, we focus on the AMCI process in marine boundary-layer stratocumulus, which is a canonical cloud regime for studying AMCI as this regime is often in an emergent state of precipitation and is sensitive to AMCI (Feingold et al. 2010; Seifert et al. 2015). In this case, an increased N_c may lead to either an increased LWC due to the suppression of precipitation (Albrecht 1989) or a reduced LWC due to enhanced entrainment of dry air (Ackerman et al. 2004). The overall effects of increasing N_c on LWC depends on the meteorology states in different cloud regimes. The suppression of precipitation may alter CFC by either increasing the cloud lifetime (Albrecht 1989) or by influencing the transitioning from open to closed Rayleigh-Bénard cells of stratocumulus (Rosenfeld et al. 2006; Wang and Feingold 2009a), or by altering mesoscale circulation and lower-level moisture convergence (Wang and Feingold 2009b). Nevertheless, response of LWP and CFC to N_c is still uncertain in both the observation and the general circulation models (GCMs). GCMs typically show a positive correlation between LWP and N_c and between CFC and N_c due to a direct reduction in the autoconversion of cloud droplets to raindrops by an increased N_c , which is parameterized for the collision-coalescence process (Ghan et al. 2016; Bellouin et al. 2020). Using large-eddy simulations (LES) with prescribed constant N_c , Seifert et al. (2015) showed that the suppression of precipitation due to increased N_c reduces CFC in trade-wind cumulus. However, this effect is compensated by the Twomey effect and the overall effect of aerosols on the albedo of cloud is small. LES with more complete and resolved physical processes, informed and constrained by observations, is needed to unravel discrepancies in GCMs regarding AMCI.

AMCI associated with marine cold-air outbreaks (CAO) is poorly understood and has been rarely studied due to the more complicated CAO cloud processes and a lack of measurements. de Roode et al. (2019) performed an LES inter-comparison of a CAO case to quantify the turbulent transport at length scales between 1 and 10 km and to study the sensitivity of the CAO to N_c and ice microphysics. Using the same microphysics scheme (Seifert and Beheng 2006) and prescribed constant N_c , the Dutch Atmospheric LES, the Max-Planck Institute for Meteorology (MPI) LES, and the PARallelized Large Eddy Simulation Model for Atmospheric and Oceanic Flows (PALM) obtained very different CFC, LWP, and surface precipitation in both magnitude and timing. They also show that a reduction of N_c results in a stronger precipitation, smaller LWP and earlier breakup of clouds, which is consistent with the findings for subtropical marine stratocumulus in Wang and Feingold (2009a). As marine CAOs are generally associated with mixed-phase clouds (Fletcher et al. 2016), the proper characterization and simulation of ice microphysics are expected to be critical for AMCI. Substantial spread

among LES models in ice water content (IWC) due to different parameterizations of ice microphysics was observed in de Roode et al. (2019). Tornow et al. (2021) examined the role of the riming process in marine CAO using LES with a prescribed single-mode lognormal aerosol-size distributions and two-moment Morrison cloud microphysics scheme. They showed that increasing a diagnostic ice nuclei particle concentration intensifies early and light precipitation, which accelerates the stratocumulus breakup. Their study showed that only a prognostic aerosol treatment produced plausible cloud regime transitions and indicated that a prognostic INP concentration is needed to capture ice multiplication near the cloud breakup that has often been observed. However, these LES studies did not explore how N_c impacted by a realistic setup of several aerosol modes and their hygroscopicity modulates LWP, CFC, and radiation fluxes during CAO. Therefore, a prognostic N_c , based on model resolved meteorology and measured aerosol size distributions and hygroscopicity, is important in understanding AMCI.

The Western North Atlantic Ocean (WNAO) region is characterized by a complicated climate system that features weather processes involving a wide range of spatial-temporal scales (Sorooshian et al. 2020). The sea surface temperature (SST) in the WNAO exhibits sharp spatial gradients due to the Gulf stream, which, together with strong wind, lead to strong surface heat fluxes within the atmospheric boundary layer (Painemal et al. 2021b). This creates ideal condition for cold air outbreak (CAO) events as investigated in Seethala et al. (2021) and Li et al. (2021). Aerosols transported from sources over the continental U.S., generated over ocean from shipping emissions and sea spray, and produced by long-range transport of smoke and dust (Corral et al. 2021; Aldhaif et al. 2020, 2021) contribute to the total aerosol number concentration in WNAO. The AMCI is poorly understood in this region, which is partly due to limited in-situ measurements of aerosol and cloud microphysical processes (Sorooshian et al. 2019). The Aerosol Cloud meTeorology Interactions oVer the western ATLantic Experiment (ACTIVATE) campaign aims to unravel AMCI in WNAO by collecting unprecedented in-situ and remote-sensing statistics of aerosols and cloud properties. To achieve this, the dual-aircraft approach is being adopted for about 150 flights (~ 600 joint total flight hours) during 2020-2022 in the WNAO region (25° – 50°N, 60° – 85°W). The lower-flying HU-25 Falcon (a minimum altitude of 150 m) focuses on measuring in-situ trace gases, aerosol, cloud properties, thermodynamics, and precipitation. The higher-flying King Air (nominal flight altitude of 9 km) simultaneously acquires remote-sensing retrievals of aerosols and clouds and deploys dropsondes to measure the meteorological states (Sorooshian et al. 2019).

We aim to study AMCI in the WNAO region by performing LES, constrained and evaluated by the ACTI-

VATE measurements. The measured aerosol size distributions and hygroscopicity, which provide a more realistic cloud condensation nuclei (CCN) pool, are fed into a two-moment microphysics scheme in the LES, compared to a fixed CCN for the prognostic N_c used in previous LES studies. To our knowledge, LES investigation of AMCI associated with CAO with realistic aerosol perturbations in the WNAO region has never been done before. Furthermore, the ameliorated understanding of AMCI and quantified aerosol-cloud relationships from LES can serve as a benchmark to evaluate and improve parameterizations of aerosol-cloud processes in global and regional models.

Using the same large-scale forcing strategy as in Endo et al. (2015), Li et al. (2021) investigated the marine boundary-layer (BL) and clouds during two CAO events (February 28 and March 1, 2020), which are characterized by strong temporally and spatially varying meteorological states in the WNAO region. It focused on the sensitivities of WRF-LES to large-scale forcing and surface heat fluxes constrained by the ACTIVATE measurements. In this companion study of Li et al. (2021), we focus on aerosol effects on clouds under the two CAO conditions. As mentioned above, we use WRF-LES with prognostic N_c based on measured aerosol properties, compare model results with the ACTIVATE cloud measurements, and evaluate cloud macrophysical properties in reanalysis products for the two CAO events reported in Li et al. (2021). The remainder of the paper is organized as follows. In section 2, we describe ACTIVATE measurements, reanalysis data, and satellite retrievals used in this study. Section 3 summarizes the WRF-LES numerical experiment setup. Section 4 discusses WRF-LES simulated aerosol effects on CAO clouds in two cases and compared to ACTIVATE measurements. Section 5 compares the LES BL structure and clouds with reanalysis and satellite retrievals. We conclude in section 6.

2. Observations, reanalysis, and satellite retrievals

a. Aerosol size distribution

Aerosol particles with diameter d between 3 – 100 nm were measured by the Scanning Mobility Particle Sizer (SMPS, TSI model 3085 differential mobility analyzer and TSI model 3776 condensation particle counter) and those with sizes larger than 100 nm were measured by the Laser Aerosol Spectrometer (LAS, TSI model 3340) equipped on Falcon HU-25. The uncertainty for both SMPS and LAS measurements is better than $\pm 10\% - 20\%$ over the submicron aerosol size range (Moore et al. 2021). The sampling frequency is 1/60 Hz and 1 Hz for SMPS and LAS, respectively.

The black dots in Figure 1 represent the aerosol size distribution averaged over Below Cloud-Base (BCB) flight legs, sampled by SMPS and LAS within the study domain (16:00-17:00 UTC) for the February 28 case. Two BCB

flight legs were performed, marked as BCB1 and BCB2, as shown in Figure A1(a) and Figure A2(a). Only particles larger than 10 nm in diameter are shown, as smaller nucleation-mode particles are not likely contributing to the population of cloud condensation nuclei at realistic supersaturations. We fit the measured aerosol size distributions using a log-normal distribution function,

$$\frac{dN}{d \ln d} = \frac{N^*}{\sqrt{2\pi} \ln \sigma} \exp \left[-\frac{(\ln d - \ln \mu)^2}{2 \ln^2 \sigma} \right], \quad (1)$$

where N^* is the total aerosol number concentration. μ and σ are the geometric median diameter and the standard deviation, respectively. The fitted parameters using three log-normal modes are listed in Table A1. The fitting is validated by comparing the number concentration integrated over the fitted lognormal distribution $\bar{N}_{\text{fit}} = \int dN$ to the measured integrated number concentration of aerosols \bar{N}_a during the BCB flight leg. The Percent Error (PE) in total particle number for the BCB1 and BCB2 legs are $(\bar{N}_{\text{fit}} - \bar{N}_a) / \bar{N}_a \times 100 = -3.7\%$ and -12.6% , respectively. The relatively low value of PE suggests that the fitting is robust.

The aerosol size distribution for the March 1 case is shown in Figure 2 and the corresponding fitted parameters and validation are listed in Table A2. The same to the February 28 case, two BCB flight legs were performed as shown in Figure A1(b) and Figure A2(b). Two and three log-normal modes are used for the fitting for BCB1 and BCB2, respectively. The fitting is robust as indicated by low values of PEs (3.1% and 1.3%). It is worth noting that \bar{N}_a from BCB2 is about 2.6 times larger than that from BCB1, which suggests a substantial spatiotemporal variation of aerosol particles below cloud-base. Without interactive aerosol sources and realistic boundary conditions, we do not expect the LES to capture the spatial variation of size distribution and hygroscopicity of aerosols. Thus a uniform size distribution and hygroscopicity is used within the simulation domain. The same aerosol treatment was used in Endo et al. (2015), who found that cloud macrophysical properties are insensitive, but cloud microphysical properties are sensitive, to aerosol hygroscopicity. However, they estimated the aerosol hygroscopicity according to the Köhler theory using the aerosol size distribution and CCN concentration. We use the direct measurement during the ACTIVATE campaign to ensure a more robust estimation of the bulk hygroscopicity of aerosols $\bar{\kappa}$ as discussed below.

b. Hygroscopicity of aerosol particles

The WRF-LES takes bulk hygroscopicity (κ) of each size mode, which can be estimated from κ and mass of each chemical component. The bulk κ of a solute aerosol particle with mixed component i is given by the simple

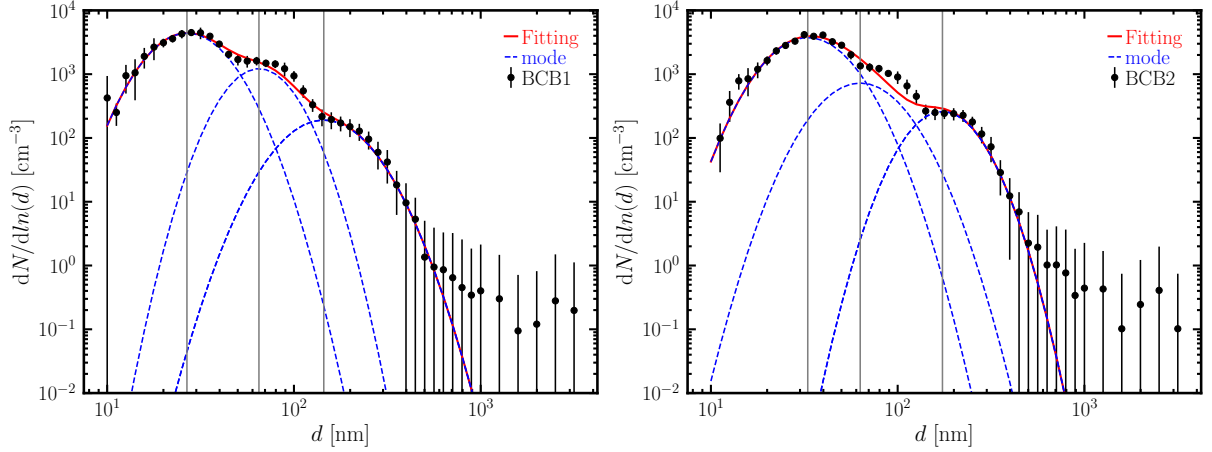


FIG. 1: Aerosol size distributions (black dots) obtained from SMPS and LAS measurements for the February 28 case during the BCB legs. The error bars indicate $\pm\sigma$ deviation from the time-averaged aerosol size distribution during a BCB flight leg. The red curve represents the final fitted size distribution. The dashed blue curves represent log-normal fitting of individual modes. Fitted parameters are listed in Table A1. Only particles with $d \geq 10$ nm are used for the fitting. The coarse mode at $d \geq 1\mu\text{m}$ is not used for the fitting because of the very low number concentrations (at least 2 orders of magnitude lower than the accumulation mode) and uncertainties (large error bars).

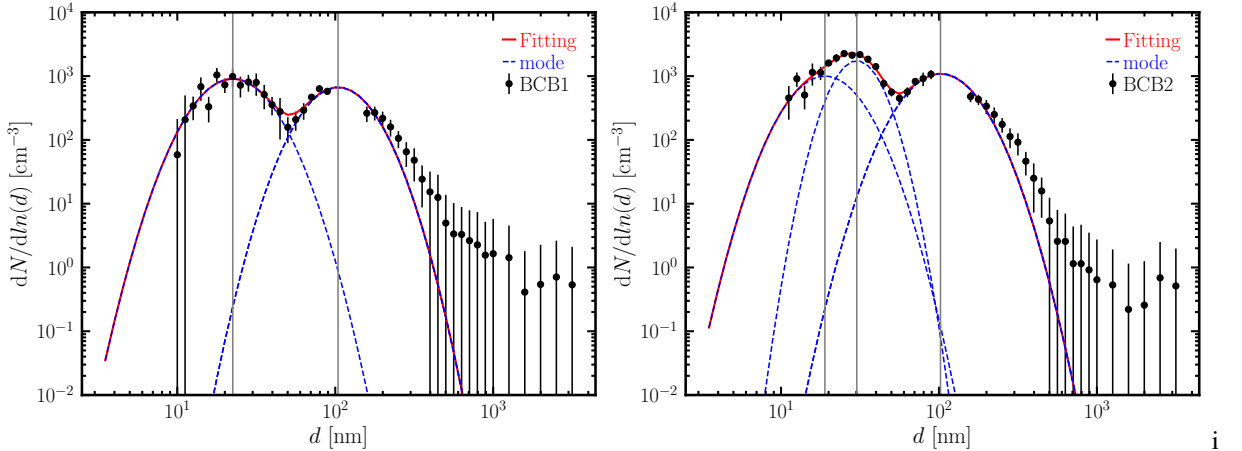


FIG. 2: Same as Figure 1 but for the March 1 case. Note that LAS measurement data for the first four bins are missing due to the failure of the laser power on March 1. Therefore they are not included in the fitting procedure.

volume mixing rule (Petters and Kreidenweis 2007)

$$\kappa = \sum_i \epsilon_i \kappa_i, \quad (2)$$

where κ_i is the hygroscopicity parameter of each individual (dry) component of aerosol particles and is obtained from Table 1 of Petters and Kreidenweis (2007) for both the non-organic and organic components. The volume fraction ϵ_i

of a component is given by

$$\epsilon_i = \frac{\frac{m_i}{\rho_i}}{\sum_i \frac{m_i}{\rho_i}}, \quad (3)$$

where m_i is the mass concentration of each component and ρ_i is the material density of each component. The mass m_i of major components was measured by an Aerodyne High Resolution Time-of-Flight Aerosol Mass Spectrometer (HR-ToF-AMS) (DeCarlo et al. 2008). The uncertainty in measured mass concentrations is up to 50% due to uncertainties in the applied instrument collection efficiency,

which was assumed to be unity for this dataset based on preliminary comparison with particle-into-liquid sampler (PILS) measurements. We take the time-averaged m_i for each BCB flight leg to calculate ϵ_i . The relative mass concentration of organic aerosol, sulfate (SO_4^{2-}), nitrate (NO_3^-), and ammonium (NH_4^+) from the AMS measurement are listed in Table A3 and the corresponding mass of $(\text{NH}_4)_2\text{SO}_4$ and NH_4NO_3 are listed in Table A4. A mass-weighted κ is calculated from AMS-measured organic, sulfate, and nitrate mass and by assuming both sulfate and nitrate are fully neutralized as $(\text{NH}_4)_2\text{SO}_4$ and NH_4NO_3 to assign appropriate κ values (Table A4). Ammonium concentrations measured by the AMS support this assumption. Time-averaged $\bar{\kappa}$ calculated according to Equation (2) is listed in the last column of Table A3. We use same $\bar{\kappa}$ for different modes of aerosol size distributions even though Fridlind et al. (2017) indicates that smaller modes have smaller kappas.

c. Droplet/ice size distribution

Cloud droplet/ice size distribution, liquid or ice water content (LWC or IWC), number concentration of cloud droplet (ice crystals) N_c (N_{ice}), and effective radius r_{eff} were measured by Fast Cloud Droplet Probe (FCDP) equipped on Falcon HU-25. The FCDP measures particles in a size range of 3 – 50 μm with an uncertainty of less than 20% (Baumgardner et al. 2017; Knop et al. 2021). The cutoff is 3.5 μm . The two-dimensional stereo (2DS) probe (Lawson et al. 2006) equipped on HU-25 measures size and concentration of cloud/ice particles in the range of 11.4 – 1464.9 μm in diameter with a spatial resolution of 11.4 $\mu\text{m}/\text{pixel}$ (Voigt et al. 2010; Bansmer et al. 2018). However, the first size bin of 2DS measurement was excluded due to large uncertainties. Therefore, 2DS measurement covers a size range of 28.5 – 1464.9 μm in the present study.

d. ERA5 and MERRA-2 reanalysis

As described in Part I (Li et al. 2021), large-scale forcings (i.e., moisture and temperature advective tendencies and wind profiles) and surface heat fluxes to drive the WRF-LES are obtained from hourly model-level and surface-level ERA5 reanalysis with a mesh grid-size of 31 km (Hersbach et al. 2020). The 3-hourly model-level and 1-hourly surface-level MERRA-2 (Gelaro et al. 2017) reanalysis with a horizontal resolution of $0.5^\circ \times 0.625^\circ$ are used to compare with WRF-LES and ERA5.

e. GOES-16 satellite retrievals

We use retrievals from the Geostationary Operational Environmental Satellite (GOES) to evaluate ERA5/MERRA-2 and WRF-LES. GOES-16 Advanced Baseline Imager (ABI) retrievals (LWP, N_c , and r_{eff}) are

produced using the Clouds and Earth’s Radiant Energy System (CERES) Edition 4 algorithms (Minnis et al. 2021; Trepte et al. 2019) adapted to geostationary satellites (Minnis et al. 2008). The GOES-16 products have a pixel size of 2 km and a selected time resolution of 20 minutes.

3. LES numerical experiment setup

The LES setup is the same as in Part I (Li et al. 2021). The lateral size of the LES domain is $L_x = L_y = 60\text{ km}$ with a grid spacing of $dx = dy = 300\text{ m}$. There are 153 vertical layers up to $z_{\text{top}} = 7\text{ km}$. The two-moment Morrison cloud microphysics scheme with prescribed aerosol size modes (see section 2.a) and hygroscopicity (see section 2.b) is employed (Endo et al. 2015). The same time-varying large-scale forcing (i.e., temperature and water vapor mixing ratio tendencies $\partial_t\theta$ and ∂_tq_v , wind speed u & v relaxation, and divergence \bar{D}) and surface heat fluxes described in Part I are adopted. To investigate the aerosol effects, we perform simulations with prescribed aerosol size distributions derived from the ACTIVATE campaign measurements as described in section 2.a. Details of simulations are listed in Table 1.

4. Aerosol-meteorology-cloud interactions

The ultimate goal of this study is to investigate how aerosols affect cloud micro-/macro-physical processes under different meteorological conditions of the two CAO cases. We first compare the cloud microphysical properties between WRF-LES and FCDP measurements. Then, aerosol effects on LWC, CFC, and radiation are investigated. Finally, we address how aerosols impact the BL meteorology.

a. Comparison of cloud microphysical properties

We start with control simulations with constant cloud droplet number concentration N_c (0228_NC and 0301_NC in Table 1), which are compared to simulations adopting prescribed aerosol size distributions derived from in-situ measurements during different BCB flight legs. The constant N_c is estimated from the FCDP measurements during the in-cloud legs of February 28 and March 1 cases. Figure 3 shows the comparison between WRF-LES and FCDP vertical profiles of LWC, $\langle N_c \rangle$, and $\langle r_{\text{eff}} \rangle$. For the February 28 case, simulation 0228_NC and 0228_NA1_ $\bar{\kappa}_{\text{org}}$ yields almost the same LWC and different $\langle N_c \rangle$ and $\langle r_{\text{eff}} \rangle$ between 16:00-17:00 UTC. By examining the corresponding statistics shown in Figure 4(a) at flight legs with sufficient statistics, it is evident that simulation 0228_NC is able to capture the vertical structure of $\langle N_c \rangle$ and $\langle r_{\text{eff}} \rangle$ while 0228_NA1_ $\bar{\kappa}_{\text{org}}$ underestimates them compared to the FCDP measurements.

The hygroscopicity of organic aerosols κ_{org} is difficult to determine due to uncertainties of their sources.

TABLE 1: List of simulations. “NC” denotes prescribed cloud droplet number concentration and “NA” denotes prescribed aerosol number concentration. BCB flight legs and $\bar{\kappa}$ are consistent with the values listed in Table A4. The mean κ of each aerosol components ($\bar{\kappa}$) is used in the simulations unless otherwise specified. 0228_NA1_ $\bar{\kappa}_{\text{org}}$ and 0228_NA1_ $\kappa_{\text{org}}^{\text{max}}$ denote the simulations with $\bar{\kappa}_{\text{org}}$ and $\kappa_{\text{org}}^{\text{max}}$, respectively. Simulations 0228_NC and 0301_NC are from Li et al. (2021).

Simulations	N_a [cm ⁻³]	N_c [cm ⁻³]	BCB leg	$\bar{\kappa}$
0228_NC	–	650	–	–
0228_NA1_ $\bar{\kappa}_{\text{org}}$	5593	–	BCB1	0.313
0228_NA1_ $\kappa_{\text{org}}^{\text{max}}$	5593	–	BCB1	0.392
0228_NA2	5364	–	BCB2	0.341
0301_NC	–	450	–	–
0301_NA1	1434	–	BCB1	0.451
0301_NA2	3100	–	BCB2	0.479

We perform two simulations (0228_NA1_ $\bar{\kappa}_{\text{org}}$ and 0228_NA1_ $\kappa_{\text{org}}^{\text{max}}$) with the same prescribed aerosol size distributions but different $\bar{\kappa}$ (due to different κ_{org}) estimated from the in-situ aircraft measurements of mass of aerosol components during the ACTIVATE campaign for the February 28 case. As discussed in section 2.b, we derive $\bar{\kappa}$ from either the mean or largest value of κ_{org} . $\kappa_{\text{org}} = 0.1$, a mean value from Table 1 of Petters and Kreidenweis (2007), is used to calculate $\bar{\kappa}$ for simulation 0228_NA1_ $\bar{\kappa}_{\text{org}}$. In simulation 0228_NA1_ $\kappa_{\text{org}}^{\text{max}}$, the upper value $\kappa_{\text{org}} = 0.229$ is adopted. As shown in Figure 3, $\langle N_c \rangle$ and $\langle r_{\text{eff}} \rangle$ from simulation 0228_NA1_ $\kappa_{\text{org}}^{\text{max}}$ are almost identical to the ones from 0228_NA1_ $\bar{\kappa}_{\text{org}}$. This is because κ of the organic component is about six times small than of the non-organic components even though the mass fraction of the organic component is 54.5%.

We then investigate how vertical profiles of $\langle N_c \rangle$ and $\langle r_{\text{eff}} \rangle$ depend on different aerosol size distributions obtained from two BCB flight legs for the February 28 case. Simulation 0228_NA2 is the same as 0228_NA1_ $\bar{\kappa}_{\text{org}}$ but with aerosol size distributions (Figure 2(b)) and $\bar{\kappa}$ derived from BCB2 (Table A1 and Table A4). Figure 3(a) shows that $\langle N_c \rangle$ and $\langle r_{\text{eff}} \rangle$ from simulation 0228_NA1_ $\bar{\kappa}_{\text{org}}$ (red dots) are very close to the ones from 0228_NA2 (blue open circles), which is due to the fact that aerosol size distributions from the two BCB flight legs are similar as shown in Figure 1. It is worth noting that the aerosol (LAS and SMPS) and FCDP measurements were not carried out simultaneously or collocated as shown in Figure A2(a) for neither BCB flight legs. Figure A1(a) shows the Falcon flight trajectory with the contour level representing the measurement time and stars and squares marking the start and end of BCB1 and BCB2 for the February 28 case. Most of the sampling of FCDP took place around 16:24 UTC (Figure A2(a)), which is closer to the BCB2 flight leg (Figure A1(a)). This suggests that the location of aerosol measurements during BCB2 is closer to the FCDP measurement than that during BCB1, which ex-

plains why $\langle N_c \rangle$ and $\langle r_{\text{eff}} \rangle$ from simulation 0228_NA2 are slightly closer to FCDP measurements than those from 0228_NA1_ $\bar{\kappa}_{\text{org}}$. Therefore, the discrepancy of $\langle N_c \rangle$ and $\langle r_{\text{eff}} \rangle$ between “NA” simulations and FCDP measurements likely depend on the collocation between the aerosol measurements and the FCDP measurements.

Figure 3(b) shows the comparison for the March 1 case. Vertical profiles from simulation 0301_NC are close to the ones from 0301_NA1. The statistics of vertical profiles from both simulation 0301_NC and 0301_NA1 agree well with the FCDP measurements as shown in Figure 5. We also perform a simulation with aerosol size distributions from BCB2 shown in Figure 2(b), the integrated aerosol number concentration (\bar{N}_a) of which is about two times larger than the one from aerosol size distributions shown in Figure 2(a). As expected, $\langle N_c \rangle$ from simulation 0301_NA2 is larger than the one from 0301_NA1 as shown in Figure 3(b). This is because the BCB1 flight leg is collocated right below the FCDP sampling while the BCB2 flight leg is not collocated well with the FCDP sampling as shown in Figure A1(b) (the contour line between stars and the thick magenta line).

We also examine the diurnal variation of cloud properties by comparing the LES with the FCDP measurements during flights from 20:47:07 to 21:10:58 UTC and from 19:43:30 to 20:13:44 UTC for the February 28 and March 1 cases, respectively. LWC from the LES and FCDP measurement agree well with each other (Figure A3(a) and Figure A4) for the February 28 case. N_c from the NA simulations capture the FCDP measurement better than the NC simulation. Interestingly, r_{eff} from the FCDP measurement is captured well by the NC simulation between 1.7–2.5 km and is closer to NA simulations above 2.5 km. For the March 1 case, the LES capture the FCDP measurements well except that it slightly underestimates r_{eff} (Figure A3(b) and Figure A5). Overall, the LES is able to capture the diurnal variation of cloud properties.

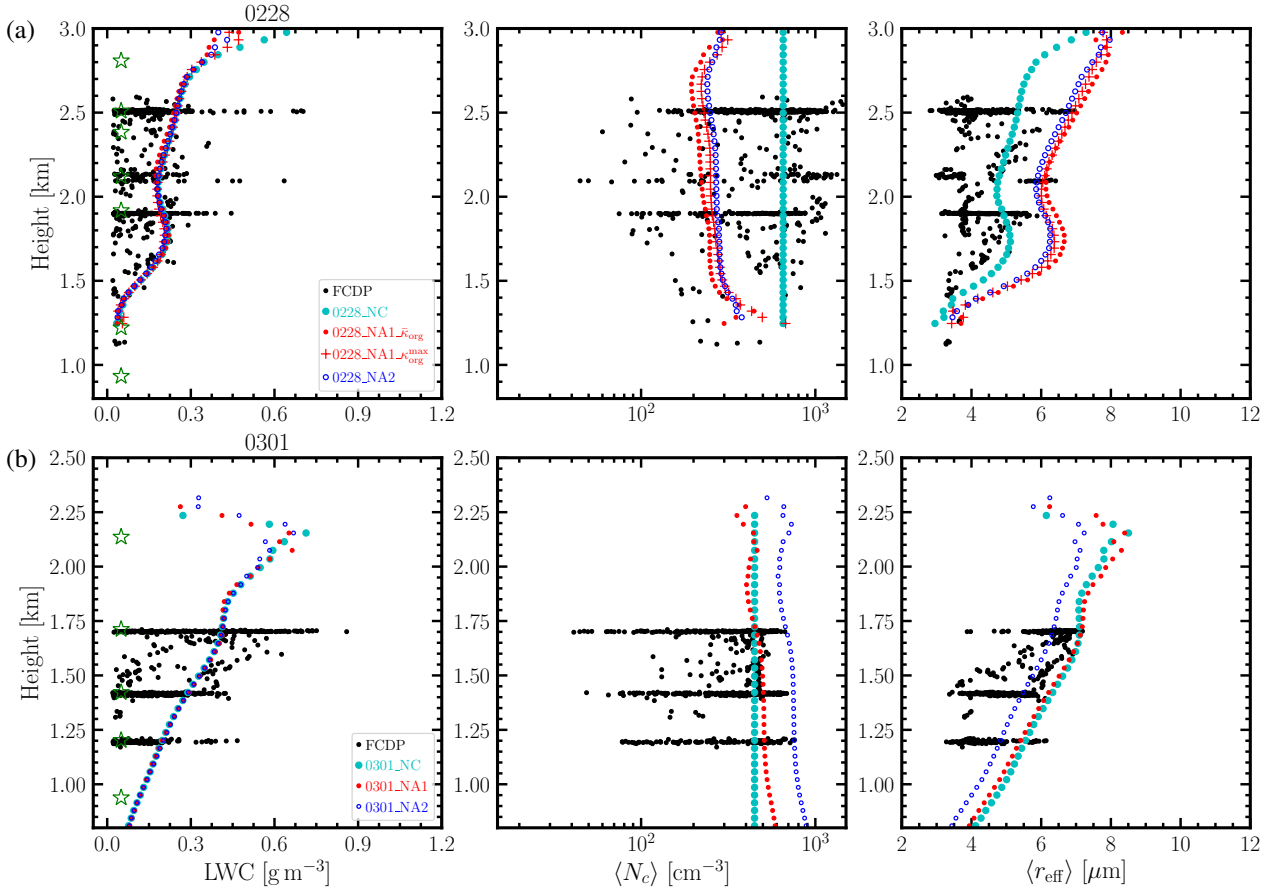


FIG. 3: Comparison of vertical profiles of LWC, $\langle N_c \rangle$, and $\langle r_{\text{eff}} \rangle$ between the WRF-LES and the FCDP sampling. A threshold of $\text{LWC} = 0.02 \text{ g m}^{-3}$, $3.5 \mu\text{m} \leq d_{\text{eff}} \leq 50 \mu\text{m}$, and $N_c = 20 \text{ cm}^{-3}$ is applied to both the WRF-LES and the FCDP sampling (black dots). For the WRF-LES, only grid cells within clouds (vertically and laterally) are averaged to obtain the vertical profile. The measurement took place between 16:00 UTC to 17:00 UTC for the February 28 and 15:00 UTC to 16:00 UTC for the March 1 cases. The corresponding mean vertical profile of LWC, $\langle N_c \rangle$, and $\langle r_{\text{eff}} \rangle$ is obtained by averaging three snapshots of WRF-LES output as the output frequency is 30 minutes. The green stars mark all the above cloud base (ACB) and below cloud top (BCT) flight legs.

b. Impact of different aerosol treatments on clouds and radiation

The comparison to in-situ cloud observations indicates that the WRF-LES simulations can reasonably capture the vertical distribution of LWC in both CAO cases. Within the aerosol measurement uncertainties, the prescribed aerosol size distributions to WRF-LES show different impacts on N_c and other cloud properties between February 28 and March 1. In both cases, the LWC shows very small sensitivity to different aerosol size distributions. Therefore, changes in r_{eff} and N_c primarily reflect the impact of aerosols on droplet nucleation, similar to the first indirect effect. Figure 6 shows the difference of vertical profiles of r_{eff} and N_c between simulation 0228_NA1_ $\bar{\kappa}_{\text{org}}$ and 0228_NC. Interestingly, both Δr_{eff} and ΔN_c exhibit

monotonic patterns vertically with a relatively larger sensitivity near cloud top. Figure 7 shows Δr_{eff} and ΔN_c for the March 1 case. Except for the large inhomogeneity at the cloud top and base, there is a different cloud droplet (number and size) response to the prescribed aerosols near cloud base.

Ice particles were observed for the March 1 case but were barely detected for the February 28 case as shown in Figure A6, where vertical profiles of IWC and $\langle N_{\text{ice}} \rangle$ from WRF-LES and 2DS measurements are shown, respectively. $r_{\text{eff,ice}}$ from 2DS sampling is also shown. Neither IWC nor $\langle N_{\text{ice}} \rangle$ are sensitive to aerosols in this case study. Figure A7 shows the corresponding statistics of IWC and $\langle N_{\text{ice}} \rangle$. $\langle N_{\text{ice}} \rangle$ from the WRF-LES agrees reasonably well with the one from the 2DS sampling while IWC is off;

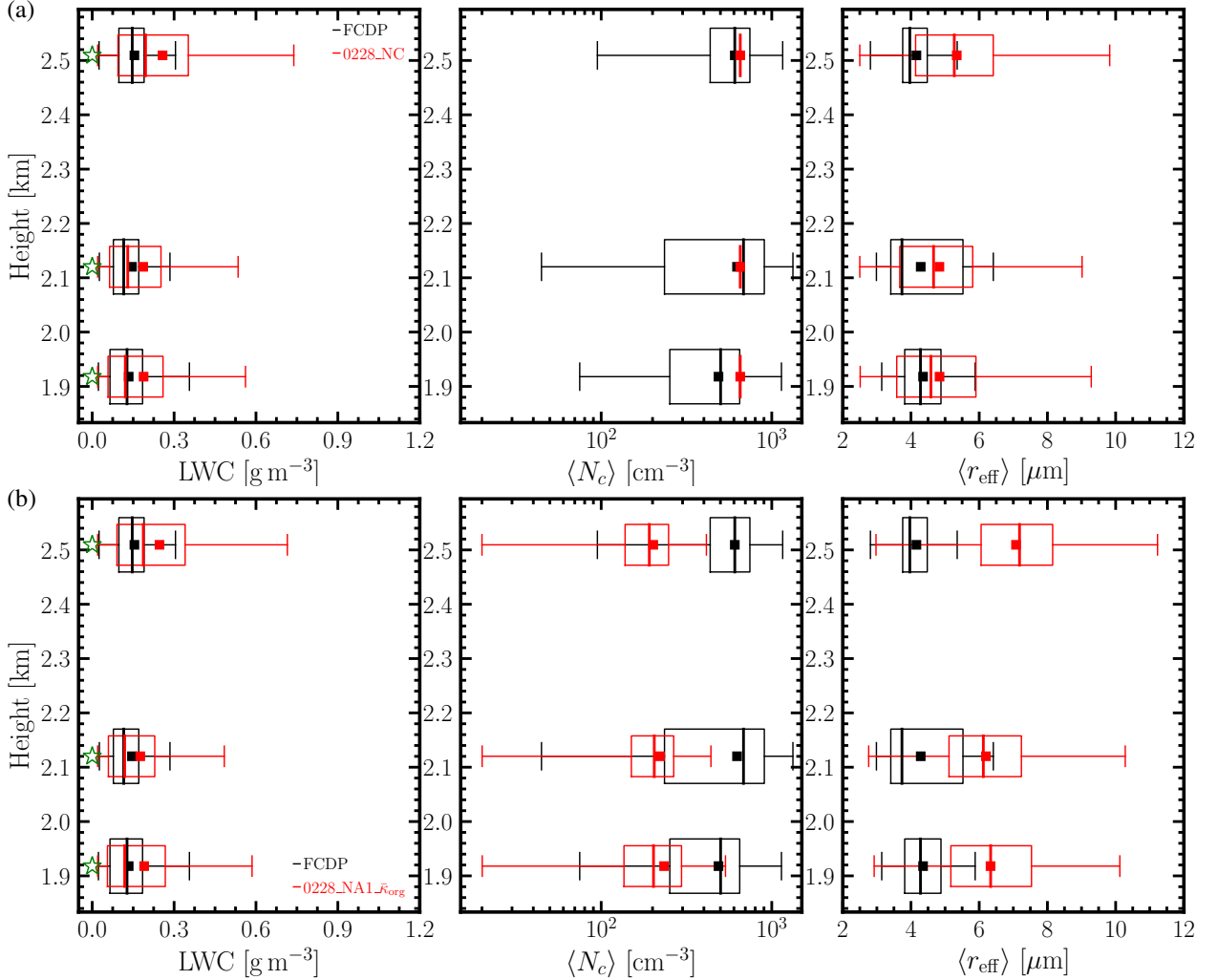


FIG. 4: Corresponding statistics of Figure 3(a) for the February 28 case with (a) constant N_c (simulation 0228_NC) and (b) constant N_a (simulation 0228_NA1_ $\bar{\kappa}_{\text{org}}$). Only flight legs (all ACB and BCT marked by green stars) within clouds that have sufficient data are used. The data are binned at those heights with a residual range of $\pm 50\text{m}$ such that at least one model layer is counted at the height of each flight legs. Smaller residual ranges does not affect the statistics. The height of the red box represents the bin width and the one of the black box is rescaled for readability. In the box-and-whisker plot, the binned data extends horizontally from the 25th (Q1, l.h.s wall of the box) to the 75th (Q3, r.h.s wall of the box) percentile with the median represented by the splitting line inside the box, the mean represented by solid squares inside the box, the minimum (Q_{\min}) and maximum (Q_{\max}) values represented by the left and right end of whiskers, respectively. Here Q denotes values of a quantity (i.e., LWC, $\langle N_c \rangle$, and $\langle r_{\text{eff}} \rangle$). The statistics of N_c are a single point as N_c is constant in (a).

however, the WRF-LES captures the higher magnitude of IWC in March 1.

To further quantitatively examine the sensitivity of cloud macro-physical properties (LWP, CFC, and IWP) and micro-physical properties (N_c and r_{eff}) to the prescribed aerosols, we compare results between simulations with prescribed N_c and aerosol size distributions. To quantify the impact of prescribed aerosols in both the sign and the mag-

nitude, we use the metric of percentage difference (PD), defined as $\text{PD} = (Q_{\text{NA}} - Q_{\text{NC}})/Q_{\text{NC}} \times 100\%$ with Q_{NC} and Q_{NA} representing quantities from the NC (baseline) and NA simulations, respectively. Q is averaged between 12:00 and 18:00 UTC. For the February 28 case, we also assess the sensitivity of cloud and radiation to κ_{org} . The time evolution of differences in liquid and ice water path, cloud fraction, $\langle N_c \rangle$, $\langle r_{\text{eff}} \rangle$, and short-wave (SW) cloud forcing

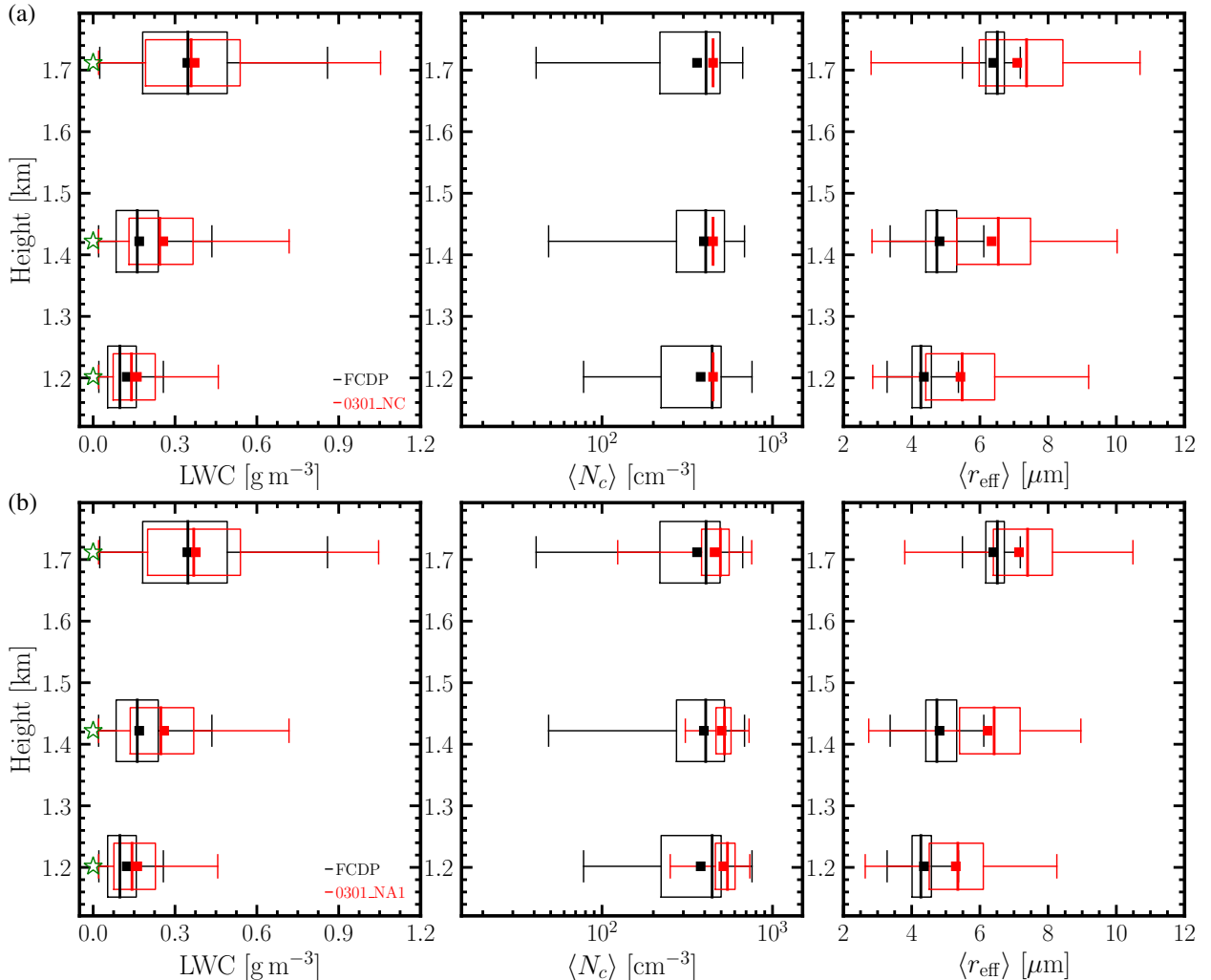


FIG. 5: Same as Figure 4 but for the March 1 case: simulation (a) 0301_NC and (b) 0301_NA1.

at the top of atmosphere (SW_{TOA}) between the control simulation 0228_NC and the ones with prescribed aerosol size distributions (0228_NA1_ $\bar{\kappa}_{org}$, 0228_NA1_ κ_{org}^{max} , and 0228_NA2) (based on different BCB flight legs) for the February 28 case is shown in Figure 8. We first examine how much NA simulations differ from the NC simulation. LWP from the NA simulations only changes slightly compared to the NC simulation (PD=-2.6%, 0.6%, and -0.5% for simulations 0228_NA1_ $\bar{\kappa}_{org}$, 0228_NA1_ κ_{org}^{max} , and 022_NA2, respectively) while IWP decreases considerably (PD=-24.8%, -11.6%, and -12.4%). The CFC also decreases (PD=-14.7%, -15.1%, and -14.9%). N_c decreases substantially (PD=-60.9%, -55.7%, and -55.0%). Correspondingly, $\langle r_{eff} \rangle$ increases (PD=27.2%, 23.8%, and 21.5%). ΔSW_{TOA} changes by $0.19 W m^{-2}$, $-0.94 W m^{-2}$, and $-0.93 W m^{-2}$ for simula-

tions 0228_NA1_ $\bar{\kappa}_{org}$, 0228_NA1_ κ_{org}^{max} , and 022_NA2, respectively.

To examine the effect of κ on these quantities, we compare simulation 0228_NA1_ $\bar{\kappa}_{org}$ and 0228_NA1_ κ_{org}^{max} . We use $\Delta PD = (Q_{NA_i} - Q_{NA_j})/Q_{NC}$ to quantify differences between NA simulations, where the subscripts NA_i and NA_j indicate two different NA simulations. ΔLWP from simulations 0228_NA1_ $\bar{\kappa}_{org}$ (red solid circles) and 0228_NA1_ κ_{org}^{max} (red pluses) starts to differ around 10:00 UTC while ΔIWP starts to differ around 15:00 UTC (Figure 8). The difference of PD between simulation 0228_NA1_ κ_{org}^{max} and 0228_NA1_ $\bar{\kappa}_{org}$ in LWP is $\Delta PD_{LWP} = (0.63 - (-2.58))\% = 3.21\%$, and in IWP is $\Delta PD_{IWP} = 13.11\%$. However, ΔCFC is almost the same with $\Delta PD_{CFC} = -0.44\%$. $\Delta \langle N_c \rangle$ and $\Delta \langle r_{eff} \rangle$ shows considerable difference between simulations 0228_NA1_ $\bar{\kappa}_{org}$

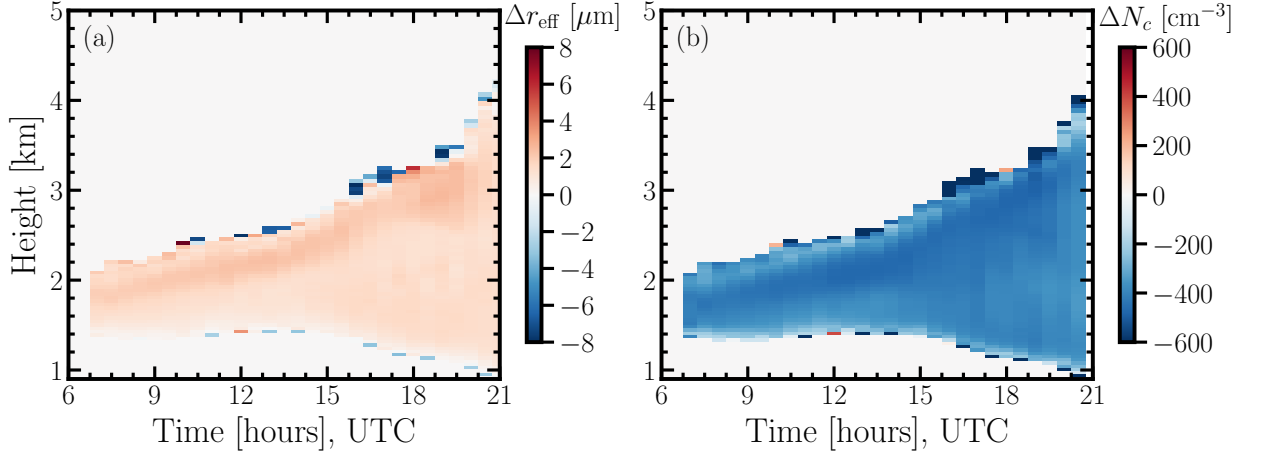


FIG. 6: Evolution of difference of (a) r_{eff} and (b) N_c profiles between simulation 0228_NA1_ $\bar{\kappa}_{\text{org}}$ and 0228_NC averaged during the dropsonde measurement time 16:00-17:00 UTC for the February 28 case.

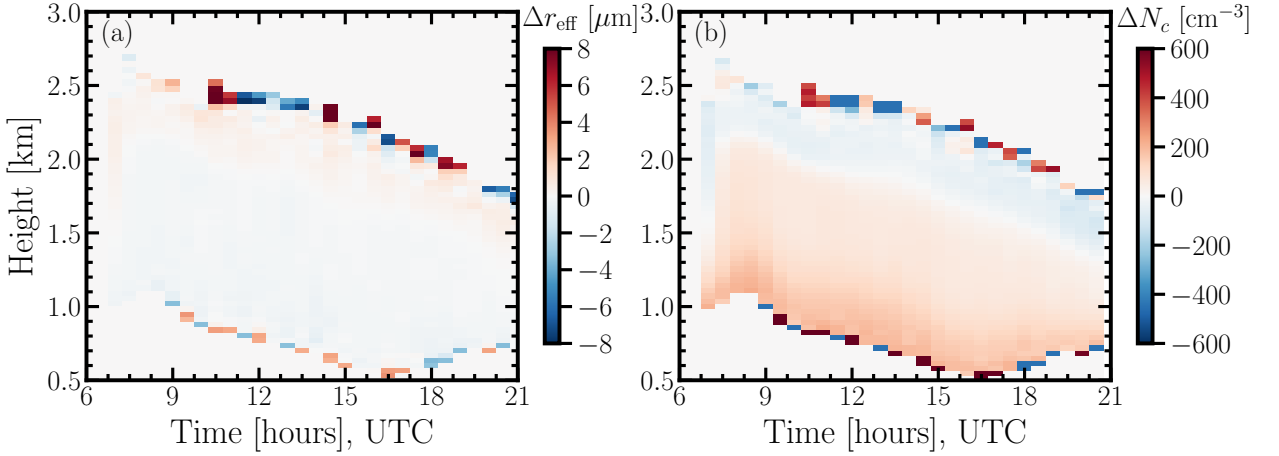


FIG. 7: Same as Figure 6 but for the March 1 case (simulation 0301_NA1 and 0301_NC averaged between 15:00 and 16:00 UTC).

and 0228_NA1_ $\kappa_{\text{org}}^{\text{max}}$ with $\Delta\text{PD}_{N_c} = 5.22\%$ and $\Delta\text{PD}_{r_{\text{eff}}} = -3.41\%$, respectively. $\Delta\text{SW}_{\text{TOA}}$ decreases by 1.13 W m^{-2} .

How cloud properties respond to aerosol size distributions from different BCB flight legs is examined by comparing simulations 0228_NA1_ $\bar{\kappa}_{\text{org}}$ (red solid circles) and 0228_NA2 (blue open circles) in Figure 8, in which aerosol size distributions from BCB2 listed in Table A1 is used. Minor differences are observed for ΔLWP ($\Delta\text{PD}_{\text{LWP}} = 1.06\%$) while considerable differences are evident for ΔIWP ($\Delta\text{PD}_{\text{IWP}} = 12.37\%$), $\langle N_c \rangle$ ($\Delta\text{PD}_{N_c} = 5.85\%$) and $\langle r_{\text{eff}} \rangle$ ($\Delta\text{PD}_{r_{\text{eff}}} = -5.74\%$). ΔCFC ($\Delta\text{PD}_{\text{CFC}} = -0.16\%$) almost has no difference. However, the magnitude of the CFC vertical-structure exhibits difference as shown in Figure A8. $\Delta\text{SW}_{\text{TOA}}$ decreases by 1.11 W m^{-2} . We further quantify the aerosol effect on radiative forcing by examin-

ing the response of cloud optical depth τ_c to cloud-top N_c via the following relation (Ghan et al. 2016),

$$\frac{\Delta \ln \overline{\tau_c}}{\Delta \ln \langle N_c \rangle} = \frac{\Delta \ln \overline{\text{LWP}}}{\Delta \ln \langle N_c \rangle} - \frac{\Delta \ln \overline{\langle r_{\text{eff}} \rangle}}{\Delta \ln \langle N_c \rangle}. \quad (4)$$

Perturbations of LWP and cloud-top r_{eff} due to N_c (cloud-top) are $\Delta \ln \overline{\text{LWP}} / \Delta \ln \langle N_c \rangle = 0.150$ and $\Delta \ln \langle r_{\text{eff}} \rangle / \Delta \ln \langle N_c \rangle = -0.269$, respectively, which leads to $\Delta \ln \overline{\tau_c} / \Delta \ln \langle N_c \rangle = 0.419$ according to Equation (4).

For the March 1 case, LWP only changes slightly with $\text{PD}=0.06\%$ and -0.02% for simulations 0301_NA1 and 0301_NA2 compared to simulation 0301_NC, respectively. PD of IWP is -0.06% and 2.34% . The CFC decreases with $\text{PD}=-3.40\%$ and -3.36% . The magnitude

of the CFC vertical-structure is quite similar as shown in Figure A9. $\langle N_c \rangle$ increases with PD=12.80% and 70.06%. $\langle r_{\text{eff}} \rangle$ decreases with PD=-1.77% and -12.77%. $\Delta \text{SW}_{\text{TOA}}$ decreases by 1.24 W m^{-2} and 0.51 W m^{-2} .

Similar to the February 28 case, ΔLWP ($\Delta \text{PD}_{\text{LWP}} = -0.51\%$) between simulations 0301_NA2 and 0301_NA1) and ΔIWP ($\Delta \text{PD}_{\text{IWP}} = 2.38\%$) in March 1 are slightly affected by different prescribed aerosol size distributions while CFC ($\Delta \text{PD}_{\text{CFC}} = -0.15\%$) is insensitive to them. Aerosol size distributions are quite different (Figure 2) between the two BCB legs (total N_a from the flight leg BCB2 is about 2.16 times larger than that of BCB1) for the March 1 case, which leads to substantial differences in $\langle N_c \rangle$ ($\Delta \text{PD}_{N_c} = 57.26\%$) and $\langle r_{\text{eff}} \rangle$ ($\Delta \text{PD}_{r_{\text{eff}}} = -11.00\%$) as shown in Figure 9. However, the difference between simulation 0301_NA2 and 0301_NA1 in $\Delta \text{SW}_{\text{TOA}}$ is only 0.72 W m^{-2} . Differences in aerosol size distribution induced susceptibility of LWP and cloud-top r_{eff} to N_c (cloud-top) are $\Delta \ln \overline{\text{LWP}} / \Delta \ln \langle N_c \rangle = -0.002$ and $\Delta \ln \langle r_{\text{eff}} \rangle / \Delta \ln \langle N_c \rangle = -0.318$, respectively, which results in a positive perturbation of $\Delta \ln \overline{\tau_c} / \Delta \ln \overline{N_c}$ (Equation (4)) of 0.316. The susceptibility of LWP and cloud-top r_{eff} to N_c (cloud-top) for both cases are summarized in Table 2. The February 28 case yields $\Delta \ln \overline{\text{LWP}} / \Delta \ln \langle N_c \rangle = 0.15$, which is close to 0.11 reported in Lee et al. (2009) and summarized in Table S1 of Glassmeier et al. (2021). Our values are very different from other LES studies reported in Table S1 of Glassmeier et al. (2021), which summarized $\Delta \ln \overline{\text{LWP}} / \Delta \ln \langle N_c \rangle$ due to precipitation or entrainment. However, we note that both the February 28 and March 1 cases represent non-precipitating stratocumulus clouds. It is also unclear whether $\Delta \ln \overline{\text{LWP}} / \Delta \ln \langle N_c \rangle$ is due to entrainment in these two cases. Overall, these two case-studies suggest that spatial-temporal variation of aerosol distributions have a profound effect on $\langle N_c \rangle$ and $\langle r_{\text{eff}} \rangle$. The effects on ΔLWP , ΔIWP , and ΔCFC are less obvious.

c. Impact of ACI on the boundary layer meteorology

The February 28 case is characterized by a warmer, drier and deeper boundary layer than the March 1 case (Li et al. 2021) as shown in Figure A10. It also shows that LES is able to capture the diurnal variation of the meteorological state (by comparing the LES to dropsonde measurements during the morning and afternoon flights as shown in Figure A10) and cloud properties for both cases. In this section, we examine how aerosols impact BL meteorology for these two contrasting CAO cases.

Differences of vertical profiles averaged within the corresponding dropsonde circle between NA and NC simulations are shown in Figure 10, where z is the altitude normalized by the cloud top height. We take simulations 0228_NA1_ $\bar{\kappa}_{\text{org}}$ and 0301_NA1 as an example. For both cases, simulations with prescribed aerosol size distributions yields larger θ (red and black curves in Figure 10(a))

and smaller q_v (Figure 10(b)) near the inversion top due to the enhanced $d\theta/dt$ (Figure 10(e)) and weakened dq_v/dt (Figure 10(f)) by condensation/evaporation, but there are quite different responses near cloud base between the two cases. This demonstrates that aerosol affects meteorological states via the case-dependent response in cloud condensation/evaporation process to aerosol perturbations. Even for the same case (0228 or 0301), different aerosol perturbations (0228_NA2 or 0301_NA2) have a different impact on the cloud and thermodynamical processes, in terms of magnitude or vertical location, as shown in the vertical profiles (gray and orange curves in Figure 10) compared to those of 0228_NA1 and 0301_NA1, correspondingly. The response evolves with time as well. The time evolution of vertical-profiles difference for the February 28 case is shown in Figure A11. The aerosol effect on θ at the inversion layer evolves from positive to negative and stays positive within the boundary layer. The opposite behavior of aerosol effect on q_v and q_c is observed. Figure A12 shows the one for the March 1 case. Unlike the February 28 case, the positive effect on θ and negative effect on q_v and q_c of aerosols persist to the end of the simulation and is more profound near the evolving cloud top as discussed. $\Delta d\theta/dt$ and $\Delta dq_v/dt$ due to condensation shows the most distinct structure at the cloud top and the cloud base. The response of TKE vertical-profiles to aerosols are more complicated. It exhibits strong spatial variations for both February 28 and March 1 cases. Overall, ACI has discernible but variable effects on the BL meteorology that depend on the BL structure and clouds.

5. Evaluating cloud micro/macro-properties in ERA5 and MERRA-2

In this section, we evaluate ERA5 and MERRA-2 reanalysis by comparing the LWP, CFC, N_c , and r_{eff} from LES and GOES-16 to those from ERA5 and MERRA-2 reanalysis. Both ERA5 and MERRA-2 provide LWP as part of their hourly single-level data. The CFC field of ERA5/MERRA-2 is defined as the maximum cloud fraction in the vertical (up to 7 km) based on the model-level LWC data with a threshold of $\text{LWC} = 0.02 \text{ g cm}^{-3}$ for cloud. Note that ERA5 and MERRA-2 provide 1-hourly and 3-hourly data (instantaneous field) for the CFC calculation, respectively. The GOES-16 LWP is corrected using the mean bias reported in Painemal et al. (2012) and Painemal et al. (2021a).

Figure 11 shows the comparison between LES, GOES-16, ERA5, and MERRA-2 for the February 28 case. LWP (Figure 11(a)) and CFC (Figure 11(b)) retrieved from GOES-16 agrees reasonably well with the LES, which boosts our confidence to evaluate the ERA5 and MERRA-2 using LES. Compared to simulation 0228_NA1_ $\bar{\kappa}_{\text{org}}$, ERA5 slightly overestimates the LWP while MERRA-2

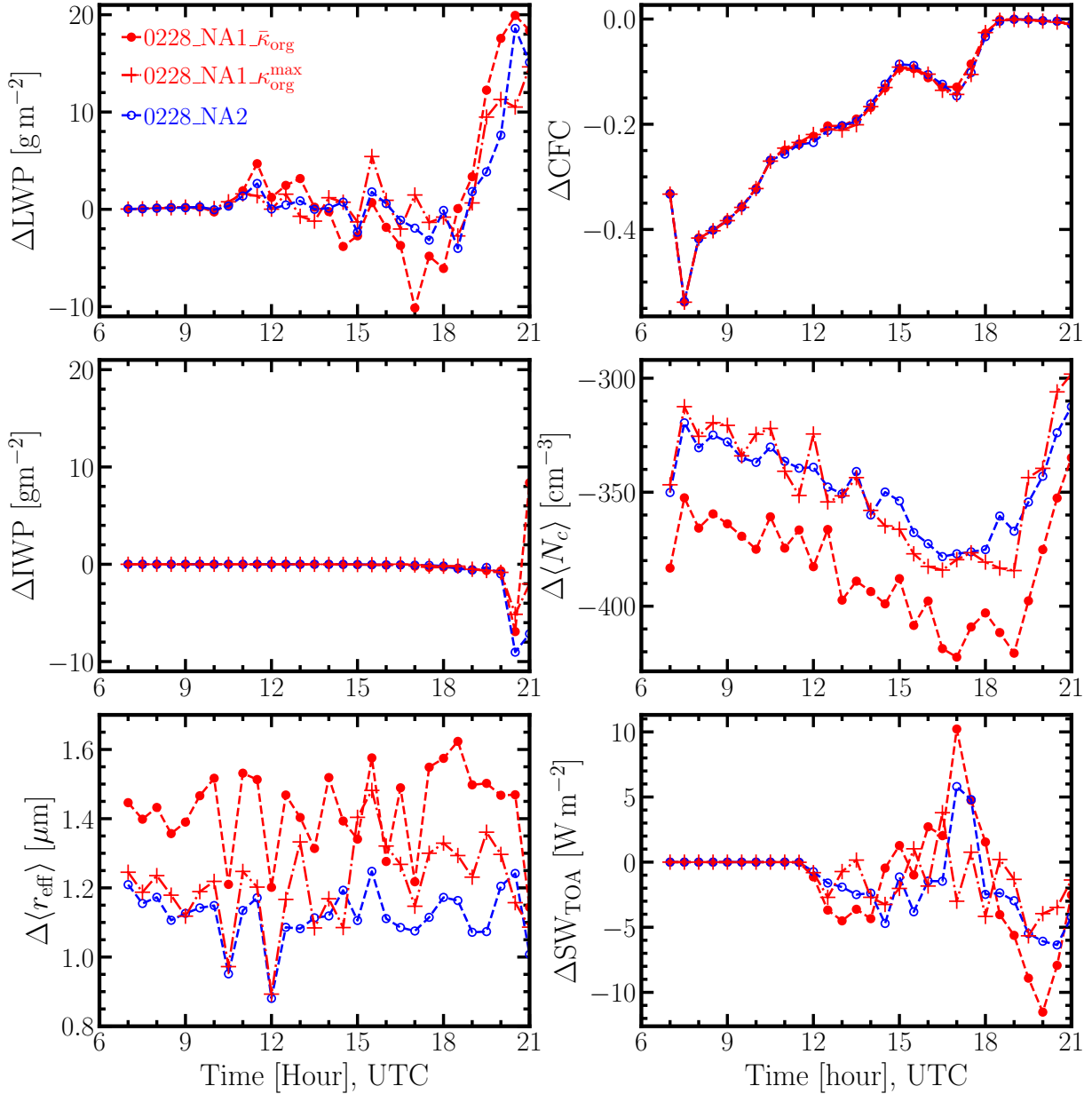


FIG. 8: Time-series differences of LWP, CFC, IWP, $\langle N_c \rangle$, $\langle r_{\text{eff}} \rangle$, and SW_{TOA} between the control simulation (0228_NC) and the ones (0228_NA1_ $\bar{\kappa}_{\text{org}}$, solid red circles; 0228_NA1_ $\kappa_{\text{org}}^{\text{max}}$, red pluses; 0228_NA2, open blue circles) with prescribed aerosol size distributions for the February 28 case. $\langle N_c \rangle$ and $\langle r_{\text{eff}} \rangle$ are averaged within clouds ($q_c \geq q_c^*$). The threshold $q_c^* = 0.02 \text{ g kg}^{-1}$ is adopted to define the cloud fractional coverage (CFC). CFC is calculated by counting the vertical columns where $q_c \geq q_c^*$, which is then normalized by the number of total vertical column of the entire domain. LWP includes liquid water and rain. IWP includes ice, graupel, and snow.

underestimates it. Nevertheless, both ERA5 and MERRA-2 capture the time evolution of LWP well. MERRA-2 has a significantly lower CFC compared to the LES, while CFC has an opposite time evolution between ERA5 and LES. We further compare the evolution of vertical structure of LWC

and CFC between ERA5, MERRA-2, and LES. As shown in Figure 12, MERRA-2 underestimates the magnitude of CFC and LWC compared to the LES. Neither MERRA-2 nor ERA5 captures the vertical structure of CFC and LWC of LES that has an apparent peak near cloud top.

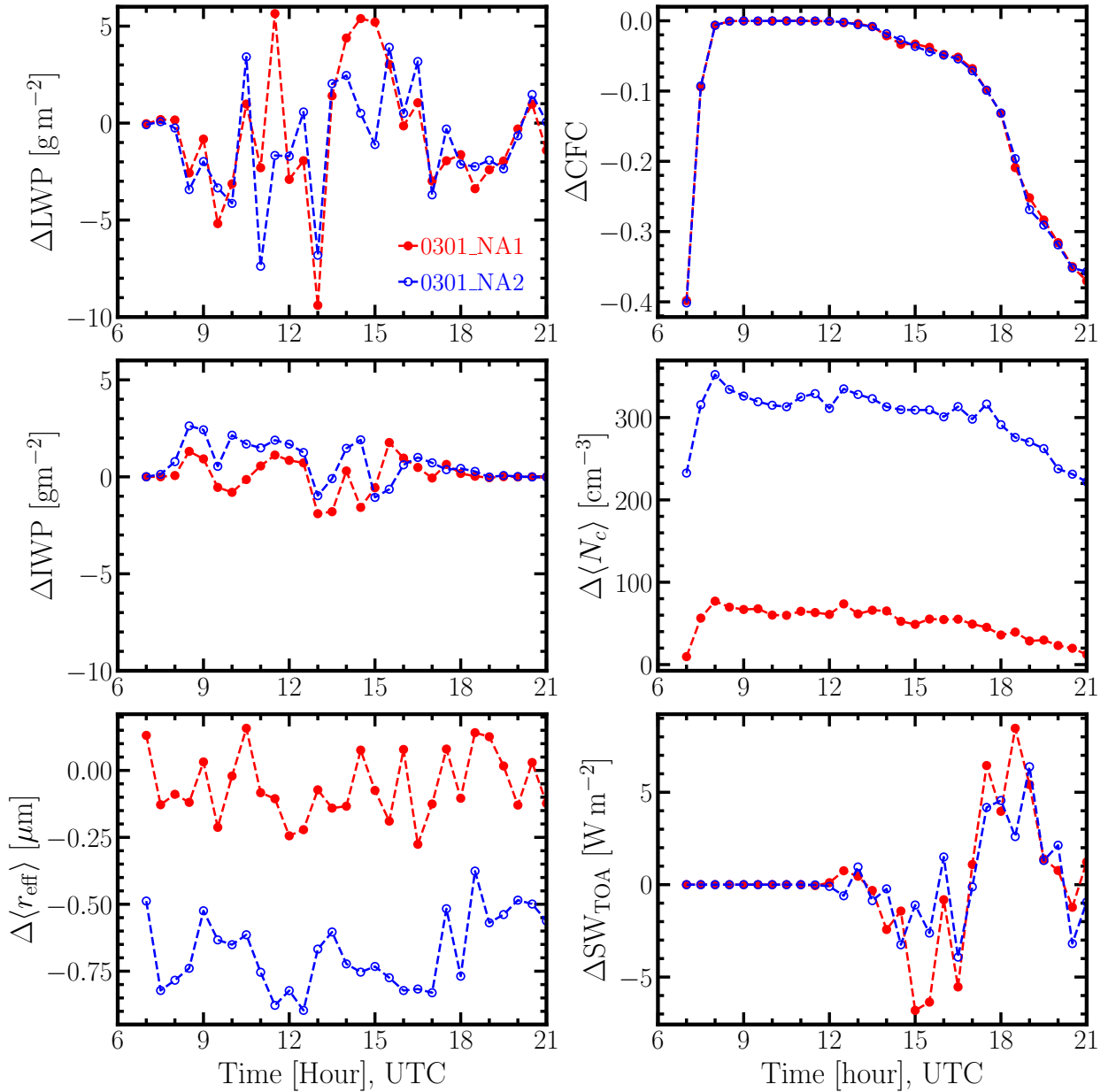


FIG. 9: Same as Figure 8 but for the March 1 case.

TABLE 2: Aerosol size distribution induced susceptibility of LWP and cloud-top r_{eff} to N_c (cloud-top) for the February 28 (0228_NA2- 0228_NA1_ $\bar{\kappa}_{\text{org}}$) and March 1 (0301_NA2- 0301_NA1) cases, respectively.

Case	$\Delta \ln \overline{\text{LWP}} / \Delta \ln \langle N_c \rangle$	$-\Delta \ln \langle r_{\text{eff}} \rangle / \Delta \ln \langle N_c \rangle$	$\Delta \ln \overline{\tau_c} / \Delta \ln \langle N_c \rangle$
February 28	0.150	0.269	0.419
March 1	-0.002	0.318	0.316

We also compare N_c and r_{eff} retrievals from GOES-16 with the LES near the top of clouds. GOES-16 N_c is derived from cloud effective radius in μm and cloud optical

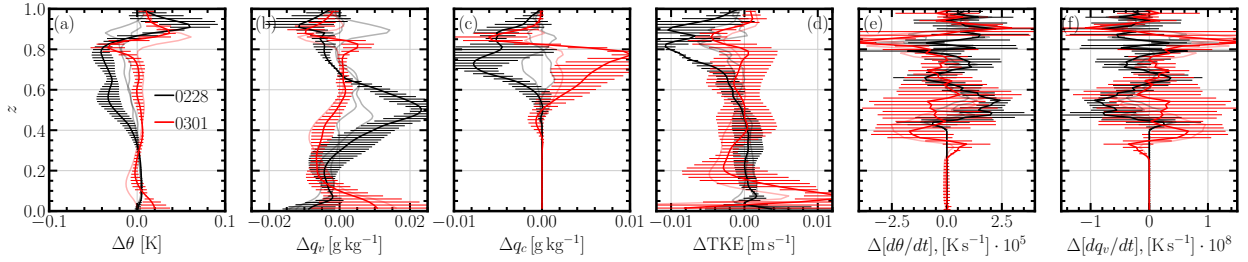


FIG. 10: Difference of vertical profiles between simulation 0228_NA1_ $\bar{\kappa}_{\text{org}}$ and 0228_NC (black curves) and between 0301_NA1 and 0301_NC (red curves) averaged during the dropsonde measurement time (16:00-17:00 UTC for the February 28 case and 15:00-16:00 UTC for the March 1 case). The error bars indicate $\pm\sigma$ deviation from the time-averaged vertical profiles. The gray and orange curves represent other simulations. z is the normalized height by the height of the cloud top. $\Delta d\theta/dt$ and $\Delta dq_v/dt$ are due to condensation/evaporation. Data is only visualized until the cloud top. The vertical profiles are shown in Figure A10.

depth τ under the adiabatic assumption. The adiabatic lapse rate of condensation Γ (g m^{-4}) is estimated from the cloud top temperature and pressure retrievals from GOES-16 (see section A5 for details of the estimation). Since several studies have shown the presence of a systematic positive bias in satellite-based r_{eff} (Painemal et al. 2012; Noble and Hudson 2015; Zhang et al. 2017; Painemal et al. 2021a), here we use values reported in Painemal et al. (2012) and Painemal et al. (2021a) for GOES-13 and GOES-16 to correct r_{eff} and, in turn, correct N_c via Equation (A1). To be consistent with the sensitivity of satellite r_{eff} to the cloud uppermost layer, N_c and r_{eff} from WRF-LES are averaged over the cloud top (4 layers, about 150 m). Figure 11(c) and Figure 11(d) show that N_c and r_{eff} from WRF-LES agree reasonably well with those from GOES-16.

Figure 13 shows the comparison between LES, GOES-16, and reanalysis for the March 1 case. The agreement in both magnitude and variation of LWP and CFC between the LES and GOES-16 is reasonably good. Compared to the LES and GOES-16, both MERRA-2 and ERA5 underestimate LWP. However ERA5 agrees better with the LES in the diurnal variation. ERA5 agrees with LES in CFC while MERRA-2 underestimates CFC. The vertical profiles of LWC and CFC are shown in Figure 14. Similar to the February 28 case, neither ERA5 nor MERRA-2 capture the vertical structure of CFC compared to LES. Nevertheless, they exhibit comparable vertical structure of LWC to the LES. ERA5 has larger CFC (nearly overcast condition) near cloud base and a LWC maximum in the middle of cloud layers. MERRA-2 has the lowest LWC and CFC at all heights. GOES-16 gives a similar N_c and r_{eff} compared to LES at the cloud top.

6. Discussions and conclusion

Using the WRF-LES, we have simulated two cold-air outbreak (CAO) cases (28 February and 1 March, 2020)

observed during the ACTIVATE campaign in the Western North Atlantic Ocean. The aerosol-meteorology-cloud interaction (AMCI) during the two CAO events are examined by comparing WRF-LES, measurements, satellite retrievals, and reanalysis.

Aerosol size distributions measured from airborne aerosol-sampling are prescribed to the LES experiments, which are compared to previous experiments with prescribed cloud droplet number concentrations (Li et al. 2021). Cloud properties from the LES experiments are then validated against the FCDP in-situ measurements. Log-normal aerosol size distributions are fitted from data acquired during two below-cloud-base (BCB) flight legs for each case. Bulk aerosol hygroscopicity estimated from mass of individual aerosol components measured by the Aerodyne Mass Spectrometer is used in the LES. For organic species, we need to make assumptions in the component hygroscopicity. To examine the effect of aerosols, we compared LES results with prescribed aerosol size distributions from different flight legs and/or with different assumptions in the estimation of bulk hygroscopicity (denoted as NA-LES) to the ones with constant cloud droplet number concentration N_c (denoted as NC-LES) obtained from the FCDP sampling. For the February 28 case, vertical profiles of LWC from the two NA-LES are in good agreement. However, N_c (r_{eff}) from the NC-LES is larger (smaller) than that from NA-LES. This is speculated to be because the aerosol sampling during the two BCB legs were not co-located very well with the FCDP sampling in space. For the March 1 case, LWC, N_c , and r_{eff} from NC-LES agree better with those from NA-LES using aerosol size distributions derived from the BCB flight leg that collocated well in space with the FCDP cloud droplet sampling. Our LES-measurement comparison also demonstrates a strong spatial and temporal variation of aerosol particle distributions during the CAO events, which adds challenges to the LES modeling and validation. By com-

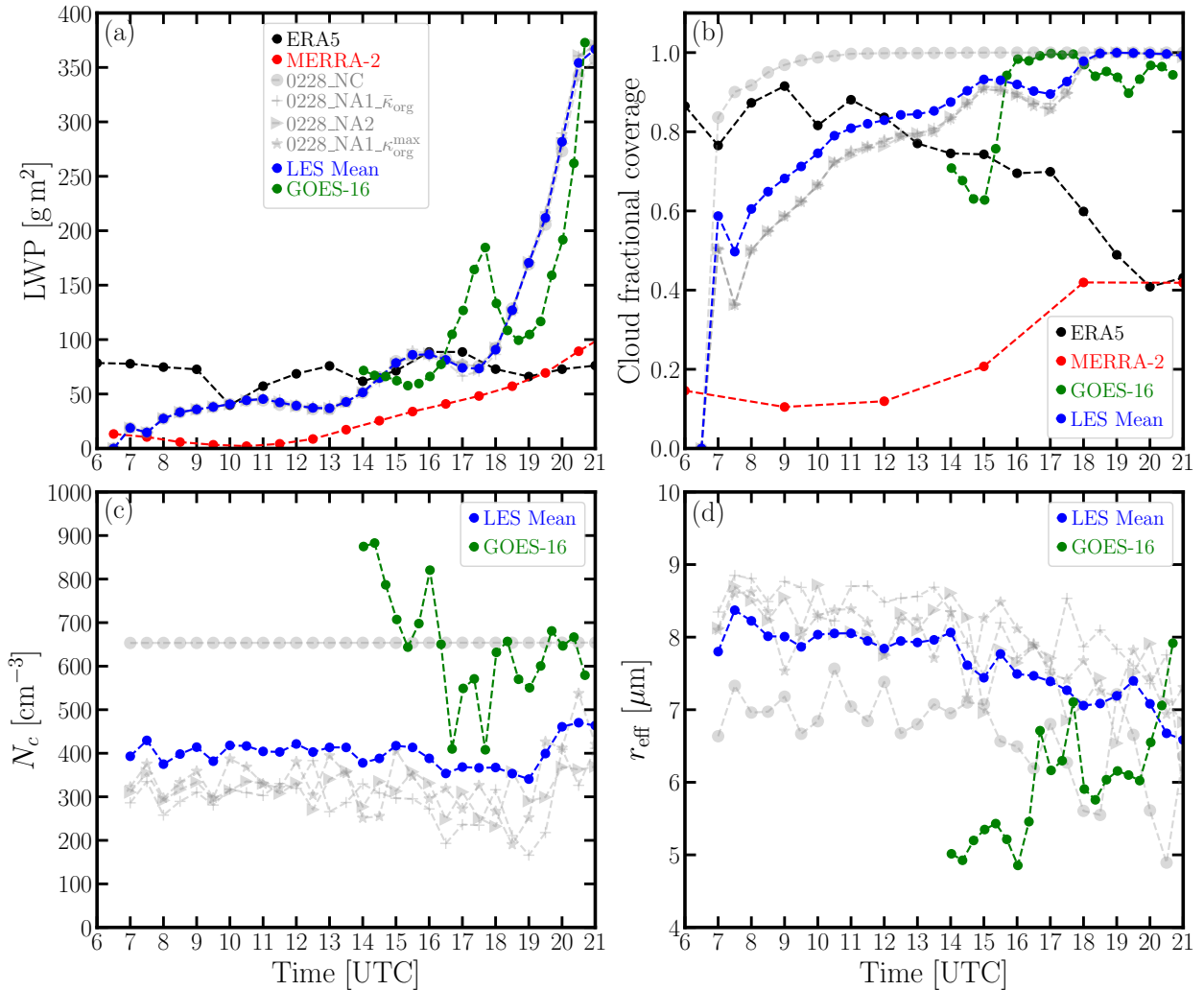


FIG. 11: Comparison between the WRF-LES (blue, averaged over all the four simulations), ERA5 (black), MERRA-2 (red), and GOES-16 (green) for the February 28 case. The gray dashed-dotted lines represent individual simulations. LWP is retrieved from hourly single-level (quantities obtained from the model level) ERA5 and MERRA-2 (starting from 00:30 UTC). The mean LWP is calculated by averaging over the dropsonde-measurement area. Both ERA5 (hourly) and MERRA-2 (3-hourly) provides Cloud Fractional Coverage (CFC) field at individual model level. The time evolution of CFC is obtained by extracting the maximum values of the CFC vertical-profiles below 7 km. Vertical profiles are obtained by sampling each layer conditionally with a threshold of $\text{LWC} = 0.02 \text{ g cm}^{-3}$ for clouds. N_c and r_{eff} are averaged over the cloud top (4 layers) from the WRF-LES output. ERA5, MERRA-2, and GOES-16 data are averaged over the dropsonde area. LWP, N_c , and r_{eff} from GOES-16 are filtered by cloud optical depth ≥ 3 . GOES-16 CFC are obtained by normalizing the number of pixels with LWP or IWP ≥ 0 by the total number of pixels within the dropsonde measurement area. To reduce the well-known systematic biases in GOES-16 retrievals, the GOES-16 LWP is corrected by the mean of the lower $+10 \text{ g m}^{-2}$ and upper $+19 \text{ g m}^{-2}$ bias bounds reported in Painemal et al. (2012) and Painemal et al. (2021a). The GOES-16 r_{eff} (N_c according to Equation (A1)) are corrected by the mean of lower $-2.4 \mu\text{m}$ and upper $-4.0 \mu\text{m}$ bias bounds according to Painemal et al. (2012) and Painemal et al. (2021a). GOES-16 data before 14:00 UTC are excluded because the retrievals are less reliable for low solar angles.

paring LES to the measurements during flights on the same day but at a later time, we show that the LES captures the diurnal variation of cloud properties for both cases. Over-

all, the good agreement between WRF-LES and measurements gives us confidence to use the LES results to study the AMCI and evaluate reanalysis for the two CAO events.

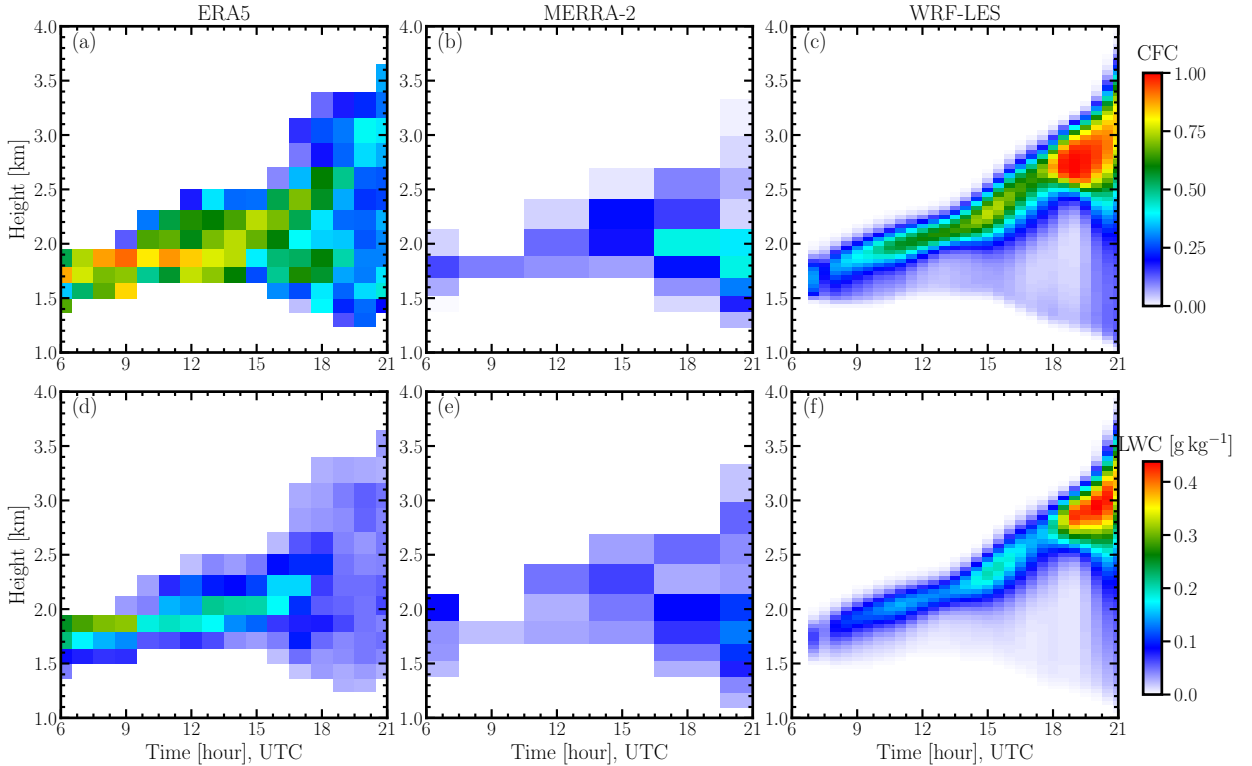


FIG. 12: Evolution of vertical profile of cloud coverage and LWC up to 7 km for the February 28 case. They are obtained by sampling each layer conditionally with a threshold of $LWC = 0.02 \text{ g cm}^{-3}$. ERA5 and MERRA-2 data are averaged over the dropsonde area. WRF-LES shows the averaged CFC from four simulations as in Figure 11.

Aerosol effects on cloud micro-physical and macro-physical properties (i.e., N_c , and r_{eff} , LWP and CFC) are investigated by comparing LES with aerosol size distributions from different BCB flight legs as input. Our use of measured aerosol size distributions to study the aerosol effects on cloud properties better represents aerosol perturbations in the study domain, which is more realistic compared to other LES studies with prognostic N_c but idealized aerosol size distribution. More importantly, LES with the same configuration and boundary/surface forcings but different aerosol perturbations allows us to disentangle the aerosol effect on clouds from the meteorological effect, which is challenging in understanding ACI (Stevens and Feingold 2009). For the February 28 case, N_c and r_{eff} are influenced by aerosols via aerosol hygroscopicity $\bar{\kappa}$ and aerosol size distributions. With the same aerosol size distributions, increasing $\bar{\kappa}$ from 0.313 to 0.392 leads to 5.2% increase (3.4% decrease) of N_c (r_{eff}). The top-of-the-atmosphere short wave radiation SW_{TOA} decreases by 1.13 W m^{-2} . LWP (IWP) increases by 3.2% (13.1%). The CFC only decreases by 0.4%. Even though aerosol size distributions from two BCB legs are quite similar, a difference of 1.11 W m^{-2} in SW_{TOA} is observed for the two

simulations. For the March 1 case, SW_{TOA} only changes by 0.72 W m^{-2} when N_a differs by a factor of about 2.6 between two BCB flight legs. The effect of N_a on LWP and CFC is negligible.

As we aim to eventually evaluate and improve ACI processes in Earth system models using LES experiments informed by the ACTIVATE observations, we have also compared our LES results to satellite retrievals (GOES-16) and reanalysis products, such as ERA5 and MERRA-2. For the February 28 case, LES and GOES-16 agree reasonably well in LWP and CFC. ERA5 captures the LWP compared with LES while MERRA-2 slightly underestimates LWP. Time evolution and the magnitude of CFC among LES, ERA5, and MERRA-2 are quite different. Both ERA5 and MERRA-2 fail to capture the vertical structure of LWC and CFC compared to the LES. For the March 1 case, LES agree well with GOES-16 in LWP and CFC. Both ERA5 and MERRA-2 underestimate the LWP compared to LES, even though the time evolution of LWP exhibit a similar trend between ERA5 and the LES. ERA5 and LES agree well in the magnitude of CFC while MERRA-2 largely underestimates it. Similar to the February 28 case, the vertical structure of LWP and CFC from MERRA-2

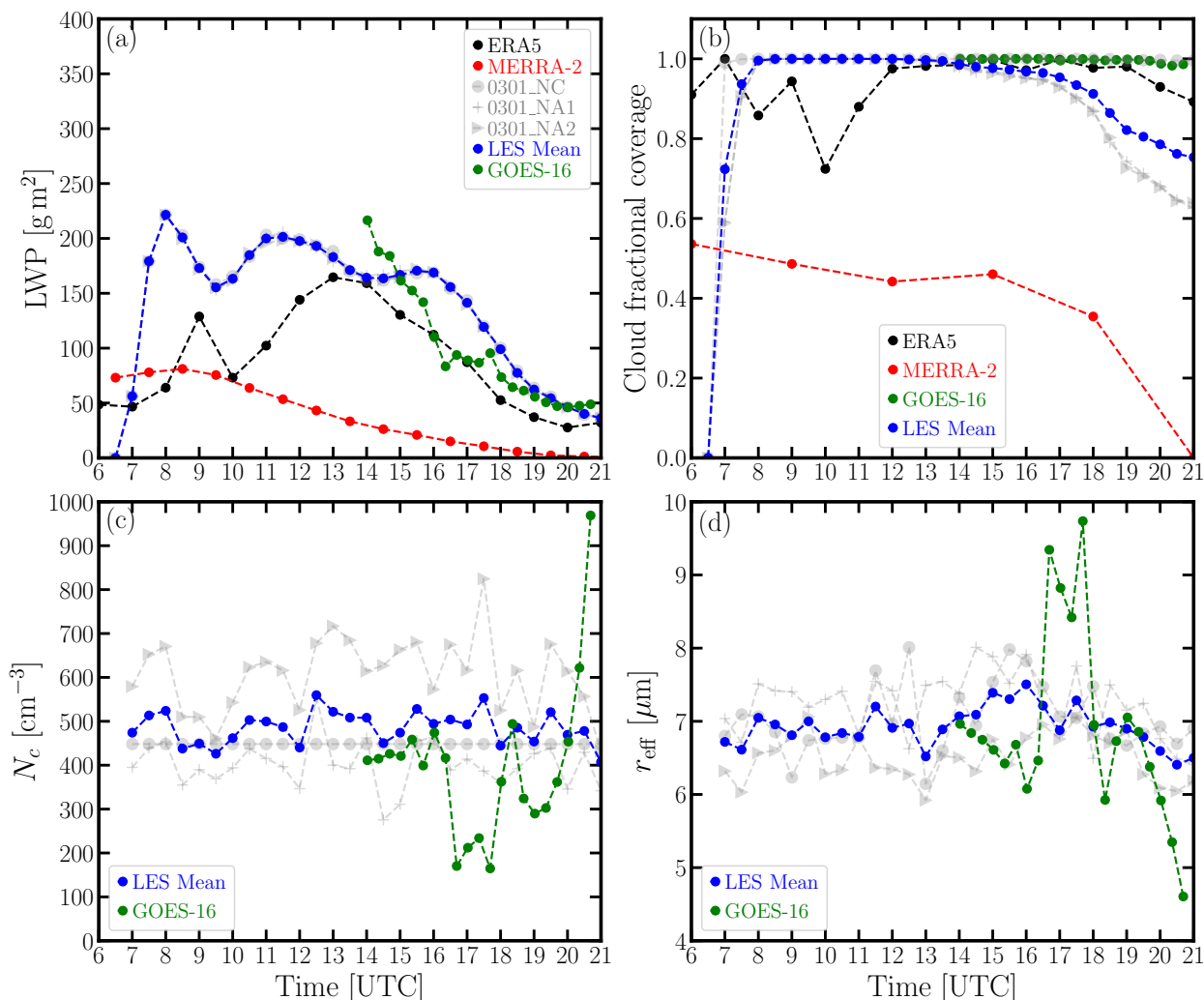


FIG. 13: Same as Figure 11 but for the March 1 case. Blue dash-dotted lines represent the mean of three simulations.

and ERA5 are quite different from the LES. We have also validated N_c and r_{eff} from the LES against the GOES-16 retrievals. For both cases, N_c and r_{eff} from the LES agrees well with those from GOES-16.

To use the LES results to evaluate AMCI in Earth system models, the next step will be to simulate these two cases using single-column configuration of Earth system models driven by the same boundary and surface forcings obtained from ACTIVATE measurements and reanalysis products.

Acknowledgments. This work was supported through the ACTIVATE Earth Venture Suborbital-3 (EVS-3) investigation, which is funded by NASA's Earth Science Division and managed through the Earth System Science Pathfinder Program Office. C.V. and S.K. thank funding by the DFG within the SPP 1294 HALO and

the TRR301-1 TP change. The Pacific Northwest National Laboratory (PNNL) is operated for the U.S. Department of Energy by Battelle Memorial Institute under contract DE-AC05-76RLO1830. The source code used for the simulations of this study, the Weather Research and Forecasting (WRF) model, is freely available on <https://github.com/wrf-model/WRF>. The simulations were performed using resources available through Research Computing at PNNL.

Data availability statement. ACTIVATE Data are publicly available at: <http://doi.org/10.5067/SUBORBITAL/ACTIVATE/DATA001>

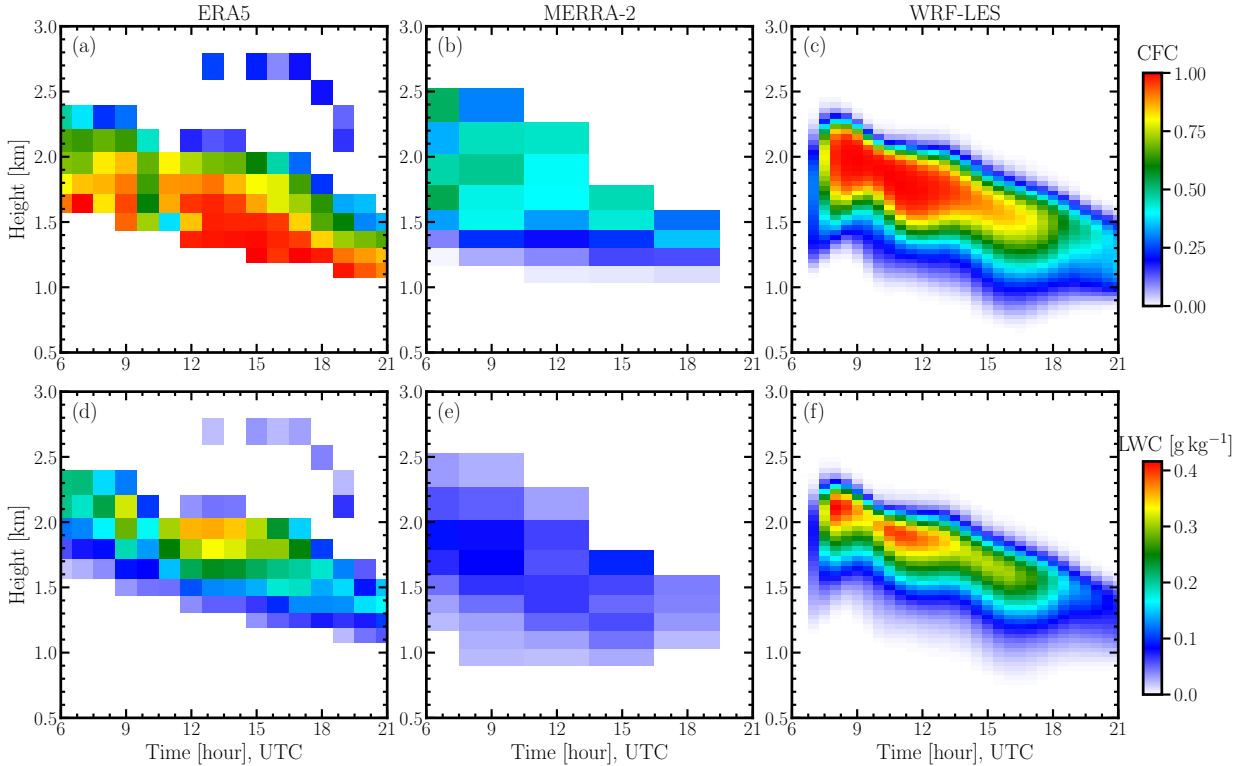


FIG. 14: Same as Figure 12 for the March 1 case. WRF-LES shows the averaged CFC from three simulations as in Figure 13.

A1. Validation of log-normal fitting of aerosol size distributions

The 3-D flight trajectories of the BCB legs for both cases are shown in Figure A1. Figure A2 shows time series of measured particle number concentration of aerosols (SMPS and LAS) and cloud droplets (FCDP) during the two BCB legs for both cases. The SMPS measurements are free from spikes, indicative of no cloud-artifacts (e.g., the cloud shattering), during the measurements. The validation of the log-normal fitting of aerosol size distributions is discussed in section 2a.

A2. Diurnal cycle of cloud properties

Figure A3 shows comparison between the FCDP measurement and LES for the two cases during the afternoon flights. The corresponding statistics are shown in Figure A4 and Figure A5 respectively.

A3. Ice

Figure A6 shows the vertical profiles of IWC, $\langle N_{\text{ice}} \rangle$, and $\langle r_{\text{eff,ice}} \rangle$. Hardly any ice was observed for the February 28 case. For the March 1 case, $\langle N_{\text{ice}} \rangle$ from WRF-LES agrees well with the 2DS measurement as shown in Figure A7.

A4. Vertical profiles

Figure A8 and Figure A9 shows the evolution of difference of CFC profiles between NA and NC simulations for the February 28 and March 1 cases, respectively.

Figure A10 shows the vertical profiles of θ , q_v , q_c , u , v , and w for the February 28 and March 1 cases. Vertical profiles from WRF-LES reproduce the observed and reanalysis profiles well for both cases. The dropsonde measurements for the two CAO cases during the ACTIVATE campaign are described in Li et al. (2021). Figure A11 and Figure A12 show the evolution of differences of vertical profiles between simulation 0228_NA1_ $\bar{\kappa}_{\text{org}}$ and 0228_NC and between simulation 0301_NA1 and 0301_NC, respectively.

A5. Retrieve N_c and r_{eff} from GOES-16

GOES-16 N_c is derived from cloud effective radius in μm and cloud optical depth τ under the adiabatic assumption (Painemal and Zuidema 2011),

$$N_c = \Gamma^{1/2} \frac{10^{1/2}}{4\pi\rho_w^{1/2}k} \tau^{1/2} r_{\text{eff}}^{5/2}, \quad (\text{A1})$$

TABLE A1: Fitted parameters of the aerosol size distribution for the February 28 case shown in Figure 1. The percentage error (PE) is defined as $PE = (\bar{N}_{\text{fit}} - \bar{N}_a) / \bar{N}_a \times 100\%$.

BCB leg	Time, UTC	N (cm^{-3})			μ (nm)			σ			\bar{N}_a (cm^{-3})	\bar{N}_{fit} (cm^{-3})	PE
		N_1	N_2	N_3	μ_1	μ_2	μ_3	σ_1	σ_2	σ_3			
BCB1	15:46:53-15:54:54	4222	994	198	26.7	64.9	144.5	1.46	1.38	1.51	5593	5384	-3.7%
BCB2	16:43:41-16:47:03	3757	723	219	33.0	63.0	173.7	1.49	1.49	1.40	5364	4690	-12.6%

TABLE A2: Fitted parameters of the aerosol size distribution for the March 1 case shown in Figure 2.

BCB leg	Time, UTC	N (cm^{-3})			μ (nm)			σ			\bar{N}_a (cm^{-3})	\bar{N}_{fit} (cm^{-3})	PE
		N_1	N_2	N_3	μ_1	μ_2	μ_3	σ_1	σ_2	σ_3			
BCB1	14:53:22-15:01:45	940	645	-	22.4	104.2	-	1.51	1.47	-	1434	1479	3.1%
BCB2	15:51:21-15:55:06	996	1192	1118	19.0	30.2	102.3	1.49	1.31	1.51	3100	3139	1.3%

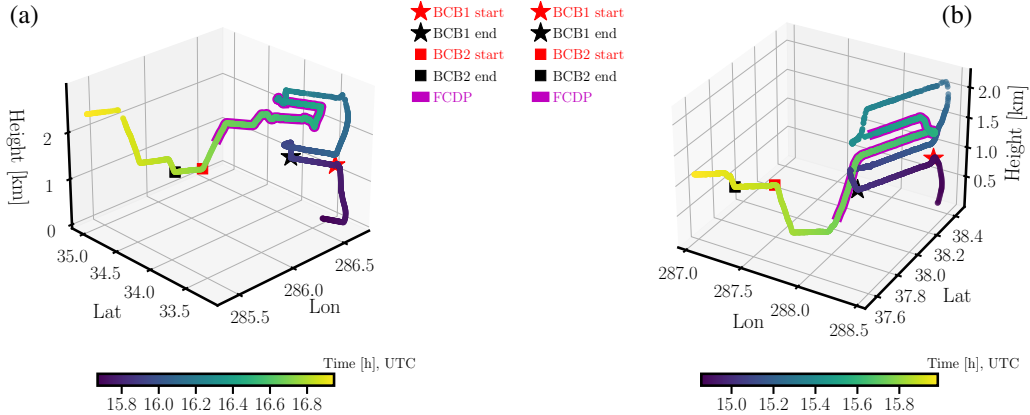


FIG. A1: Flight trajectory during the FCDP measurement for (a) the February 28 and (b) March 1 cases. Red and black stars (squares) represent the start and end of the BCB1 (BCB2) flight leg, respectively. Trajectories with most dense FCDP-sampling (16.3-16.7 and 15.45-15.75 UTC for the February 28 and March 1 cases, respectively) are highlighted as thick magenta curves.

TABLE A3: Time-averaged mass concentration \overline{m}_i from the AMS measurement sampled during BCB flight legs for the February 28 (0228) and March 1 (0301) cases. NaCl is not efficiently sampled by AMS because it is refractory (i.e., not volatile at 600 Pa), and therefore the Cl mass is likely not representative of NaCl mass. It is justified by the lack of coarse-mode number concentration in Figure 1 and Figure 2.

Component		organic	Sulfate (SO_4^{2-})	Nitrate (NO_3^-)	Ammonium (NH_4^+)
0228	BCB1	54.5%	23.4%	10.8%	10.0%
	BCB2	48.6%	25.9%	10.8%	13.9%
0301	BCB1	27.6%	46.6%	3.4%	21.3%
	BCB2	24.9%	28.5%	23.2%	22.6%

where Γ (g m^{-4}) is the the lapse rate due to condensation of water vapor and is estimated from the cloud top temperature and pressure retrievals of GOES-16. $\rho_w = 1000 \text{ kg m}^{-3}$ is the density of water. $k = r_v^3 / r_{\text{eff}}^3 = 0.8$ is

assumed to be a constant with r_v the volume mean radius. N_c is assumed to be height independent in Equation (A1).

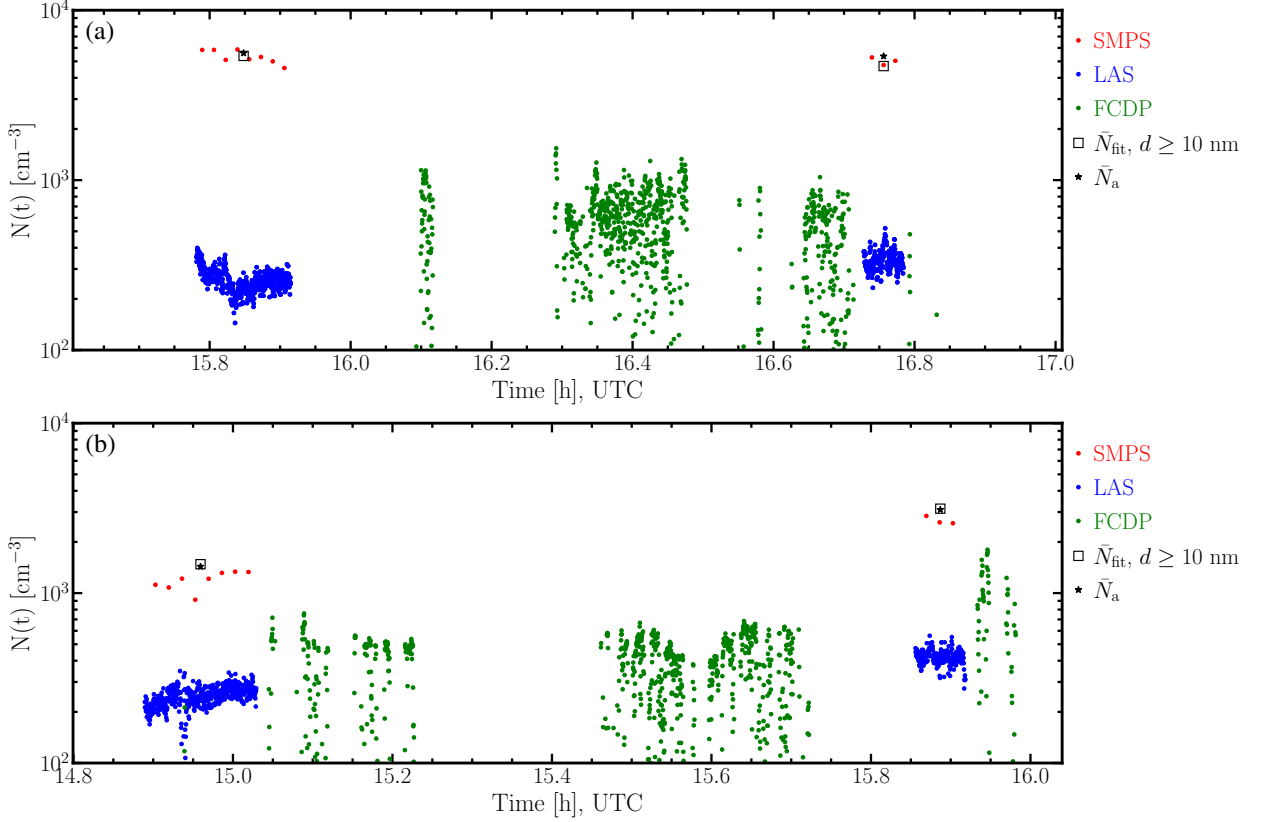


FIG. A2: Comparison between \bar{N}_a (black star), \bar{N}_{fit} (black square), and N_{FCDP} (green dots) for (a) the February 28 and (b) March 1 case. Red and blue dots represent N_a from SMPS and LAS measurements, respectively.

TABLE A4: $\bar{\kappa}$ (time-averaged κ) calculated according to Equation (2) with AMS-measured \bar{m}_i as input listed in Table A3. κ_i is adopted from Table 1 of Petters and Kreidenweis (2007) for both the non-organic components and the organic one. The mass of NH_4^+ is divided to $(\text{NH}_4)_2\text{SO}_4$ and NH_4NO_3 by its molecular proportion assuming both sulfate and nitrate are fully neutralized as $(\text{NH}_4)_2\text{SO}_4$ and NH_4NO_3 . Taking the upper limit of the kappa value for the organic aerosols as $\kappa_{\text{org}} = 0.229$ during the BCB1 sampling for the February 28 case, we get $\bar{\kappa} = 0.392$.

Component		organic	$(\text{NH}_4)_2\text{SO}_4$	NH_4NO_3	$\bar{\kappa}$
ρ_i (g cm^{-3})		1.35	1.77	1.72	
κ_i		0.1	0.61	0.67	
0228	BCB1	54.5%	30.0%	14.1%	0.313
	BCB2	48.6%	35.1%	15.5%	0.341
0301	BCB1	27.6%	60.8%	10.5%	0.451
	BCB2	24.9%	43.5%	30.7%	0.479

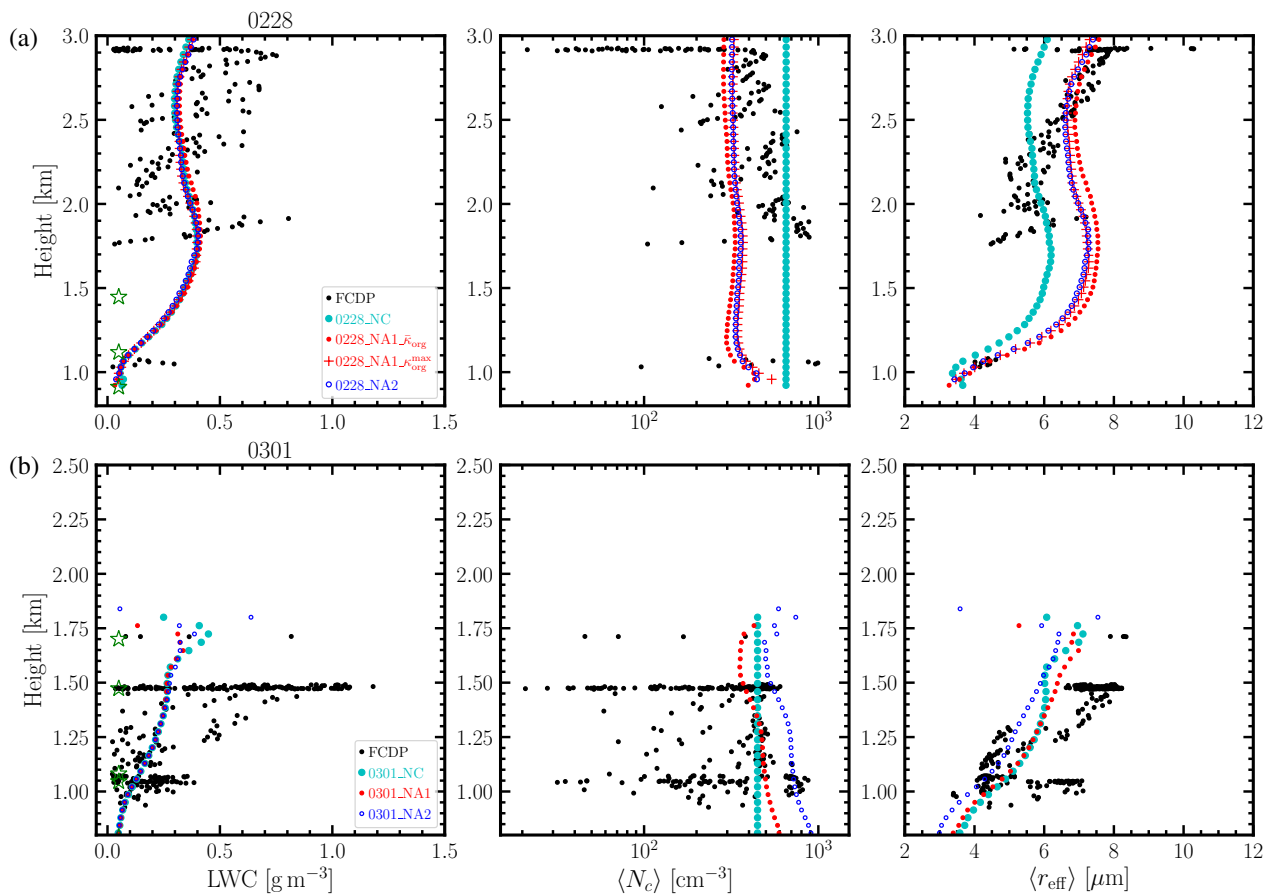


FIG. A3: Same as Figure 3 but for the flights (a) from 20:47:07 to 21:10:58 UTC and (b) from 19:43:30 to 20:13:44 UTC for the February 28 and March 1 cases, respectively.

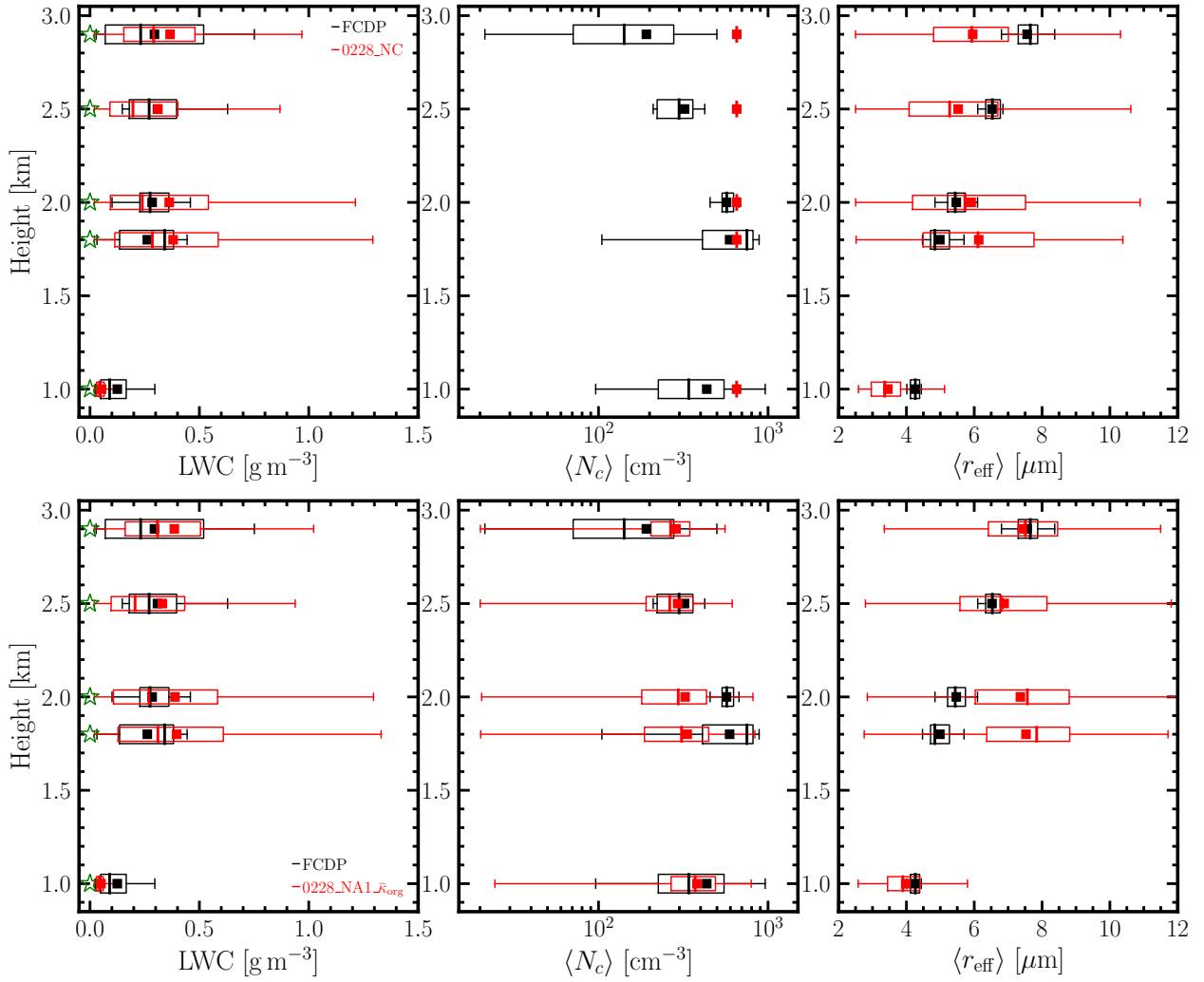


FIG. A4: Same as Figure 4 but for the measurements from 20:47:07 to 21:10:58 UTC.

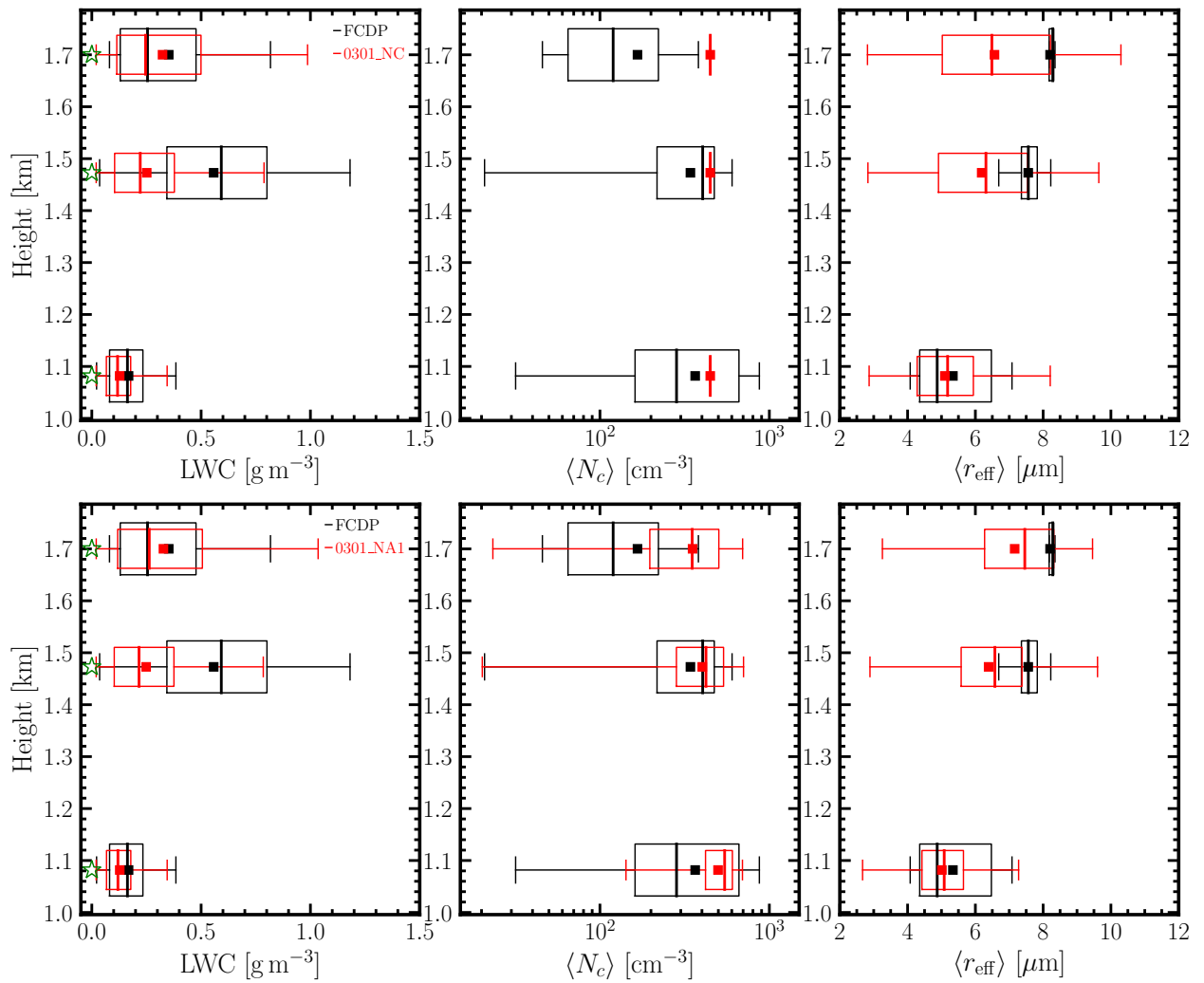


FIG. A5: Same as Figure 5 but for the measurements from 19:43:30 to 20:13:44 UTC.

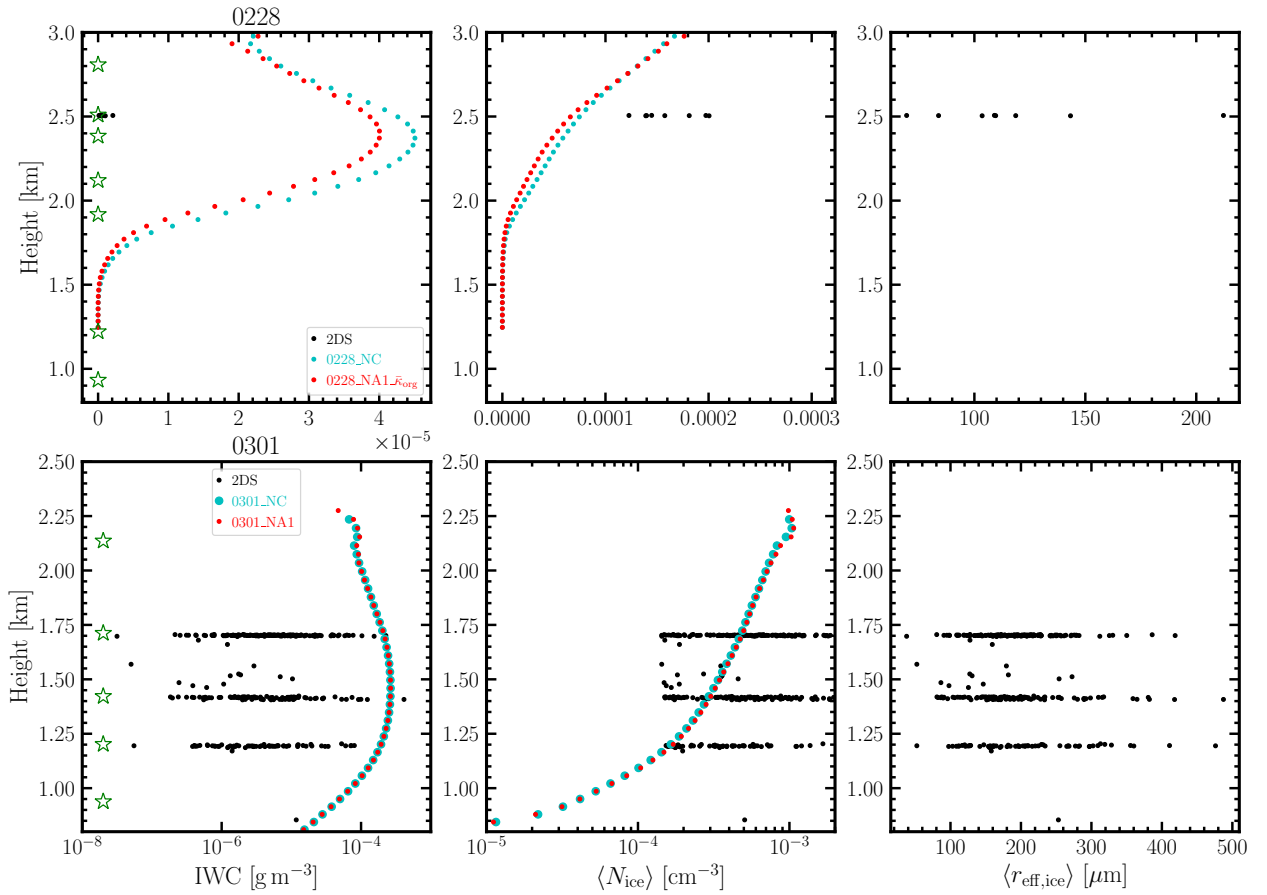


FIG. A6: Comparison between the WRF-LES and the 2DS measurement of ice particles. The IWC from WRF-LES only includes ice particles. WRF-LES does not output $r_{\text{eff,ice}}$. The $r_{\text{eff,ice}}$ is the largest radius from the 2DS measurement.

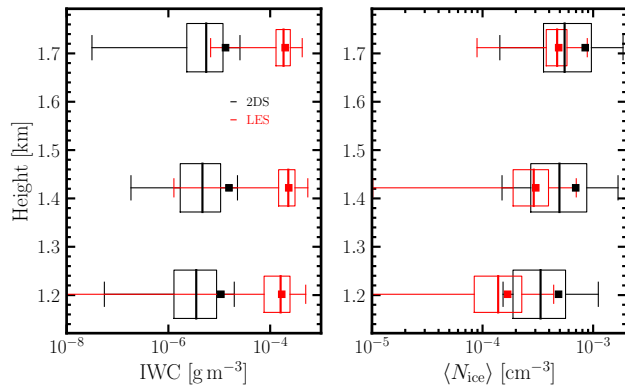


FIG. A7: Corresponding statistics of Figure A6. 2DS measurement for the March 1 case for prescribed N_a . The same criterion and procedure for the box-and-whisker plot as in Figure 4 are used. The green stars mark the altitude of flight legs.

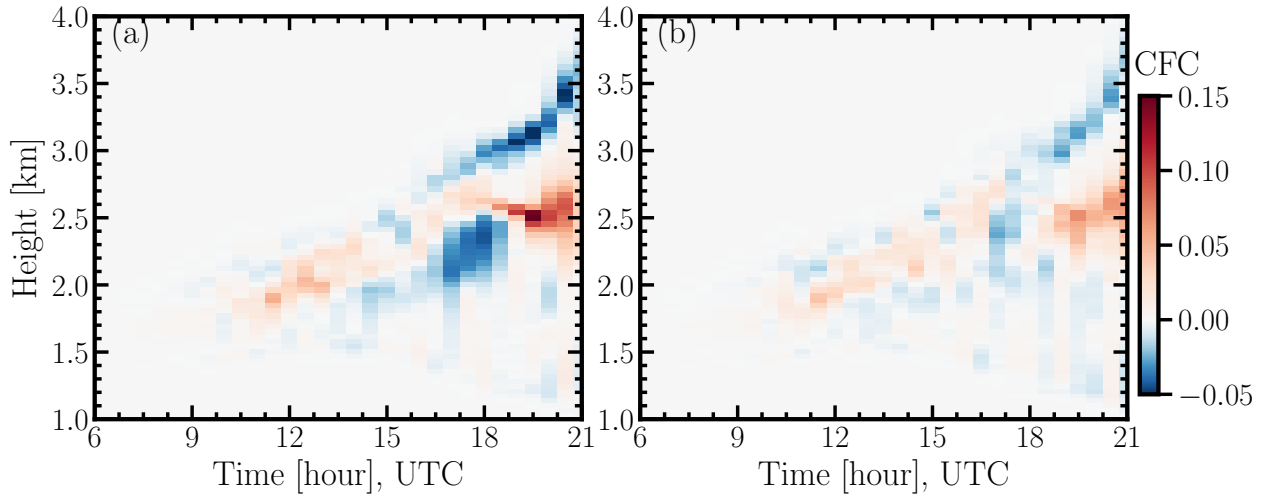


FIG. A8: Evolution of difference of CFC profiles between simulation (a) 0228_NA1_ \bar{k} _orig and 0228_NC and between (b) 0228_NA2 and 0228_NC averaged during the dropsonde measurement time 16:00-17:00 UTC for the February 28 case.

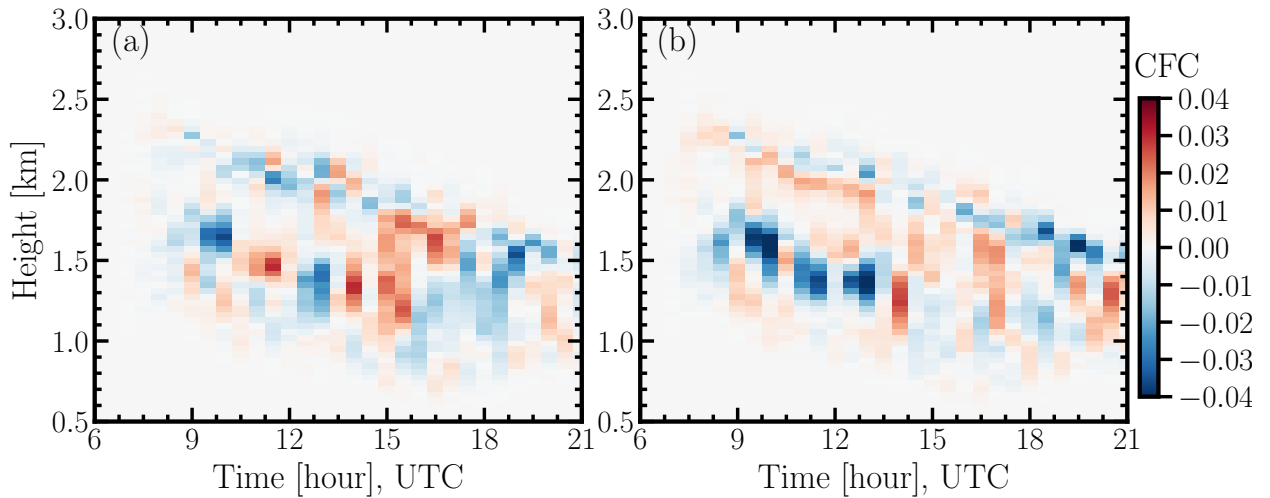


FIG. A9: Same as Figure A8 but for the March 1 case: difference between (a) 0301_NA1 and 0301_NC and between (b) 0301_NA2 and 0301_NC averaged over 15:00-16:00 UTC.

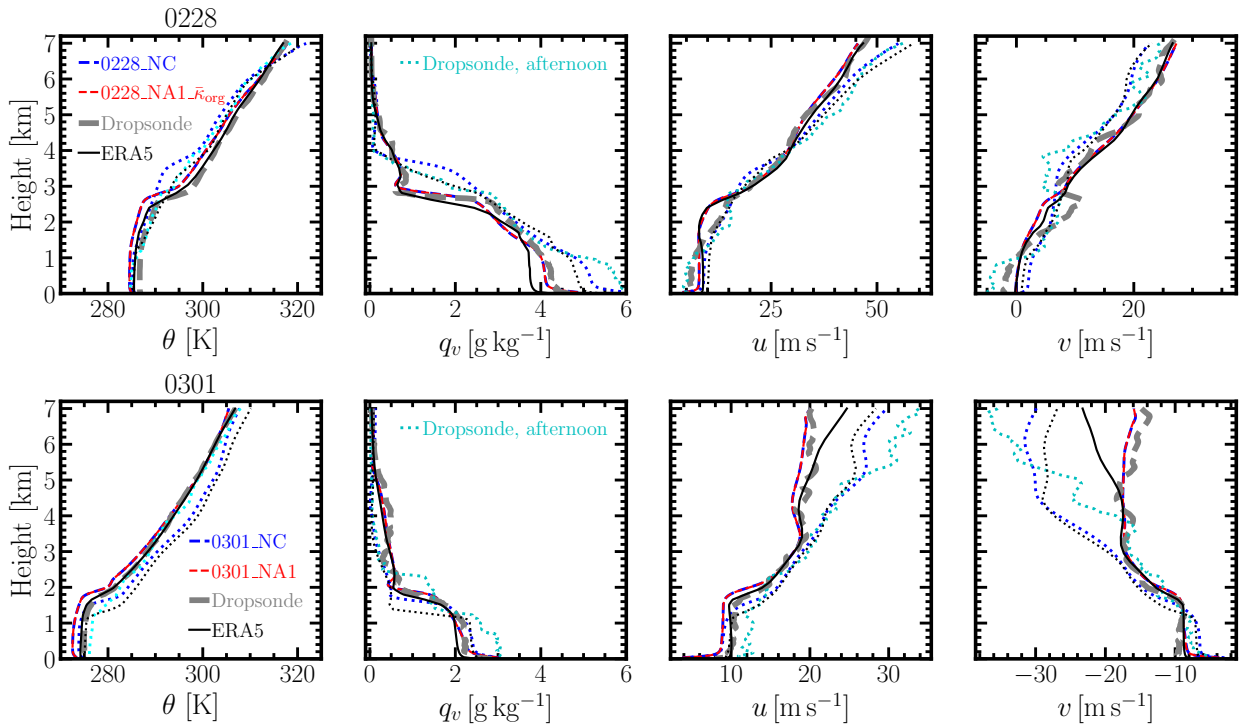


FIG. A10: Comparison of vertical profiles among dropsonde measurements (grey dashed and cyan dotted lines, averaged over all dropsondes during the morning flight), WRF-LES (blue and red dashed lines, domain averaged), and ERA5 reanalysis (black solid lines, dropsonde center of the morning flight) averaged during the morning measurement time for the February 28 (upper panel) and March 1 (lower panel) cases. Dotted lines (with the corresponding colors for ERA5 and LES) represent the ones for the afternoon flights and only vertical profiles of NC simulations are shown. 11 and 2 dropsondes are released for the morning and afternoon flights, respectively. The dropsondes location of the morning and afternoon flights are slightly different. Therefore, the vertical profiles between the morning and afternoon flights are not quantitatively comparable. Same simulations as in Figure 10. See Table 1 for the details of the simulations.

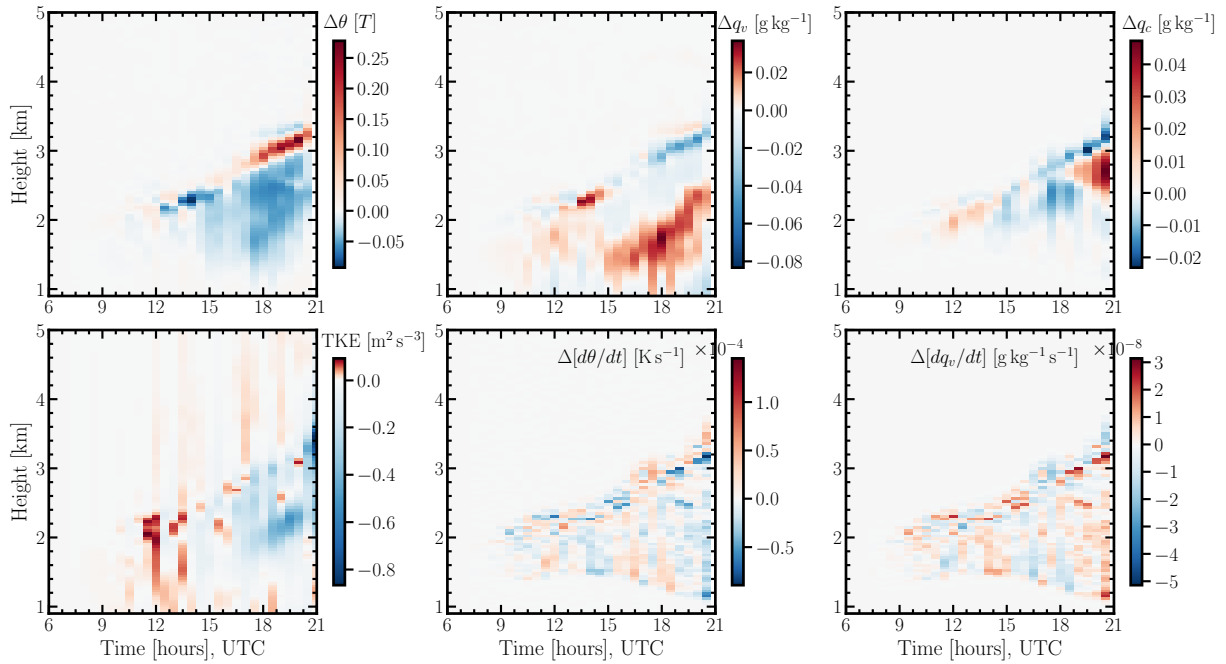


FIG. A11: Evolution of differences of vertical profiles between simulation 0228_NA1_ $\bar{\kappa}_{\text{org}}$ and 0228_NC. Same simulations as in Figure 10.

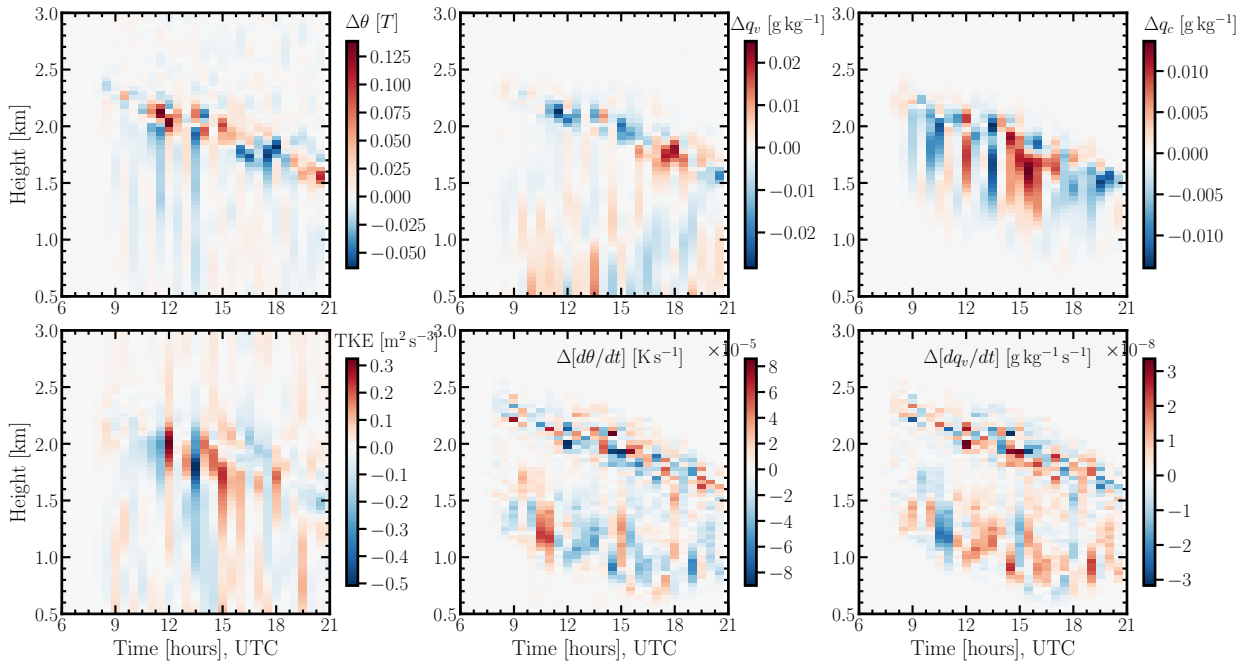


FIG. A12: Evolution of differences of vertical profiles between simulation 0301_NA1 and 0301_NC. Same simulations as in Figure 10.

References

- Ackerman, A. S., M. P. Kirkpatrick, D. E. Stevens, and O. B. Toon, 2004: The impact of humidity above stratiform clouds on indirect aerosol climate forcing. *Nature*, **432** (7020), 1014–1017.
- Albrecht, B. A., 1989: Aerosols, cloud microphysics, and fractional cloudiness. *Science*, **245** (4923), 1227–1230.
- Aldhaif, A. M., D. H. Lopez, H. Dadashazar, D. Painemal, A. J. Peters, and A. Sorooshian, 2021: An aerosol climatology and implications for clouds at a remote marine site: Case study over bermuda. *Journal of Geophysical Research: Atmospheres*, **126** (9), e2020JD034038, <https://doi.org/https://doi.org/10.1029/2020JD034038>.
- Aldhaif, A. M., D. H. Lopez, H. Dadashazar, and A. Sorooshian, 2020: Sources, frequency, and chemical nature of dust events impacting the united states east coast. *Atmospheric Environment*, **231**, 117456.
- Bansmer, S. E., and Coauthors, 2018: Design, construction and commissioning of the braunschweig icing wind tunnel. *Atmospheric Measurement Techniques*, **11** (6), 3221–3249.
- Baumgardner, D., and Coauthors, 2017: Cloud ice properties: In situ measurement challenges. *Meteorological monographs*, **58**, 9–1.
- Bellouin, N., and Coauthors, 2020: Bounding global aerosol radiative forcing of climate change. *Reviews of Geophysics*, **58** (1), e2019RG000660.
- Corral, A. F., and Coauthors, 2021: An overview of atmospheric features over the western north atlantic ocean and north american east coast—part 1: Analysis of aerosols, gases, and wet deposition chemistry. *Journal of Geophysical Research: Atmospheres*, **126** (4), e2020JD032592.
- de Roode, S. R., and Coauthors, 2019: Turbulent transport in the gray zone: A large eddy model intercomparison study of the constrain cold air outbreak case. *Journal of Advances in Modeling Earth Systems*, **11** (3), 597–623.
- DeCarlo, P., and Coauthors, 2008: Fast airborne aerosol size and chemistry measurements above mexico city and central mexico during the milagro campaign. *Atmospheric Chemistry and Physics*, **8** (14), 4027–4048.
- Endo, S., and Coauthors, 2015: Racoro continental boundary layer cloud investigations: 2. large-eddy simulations of cumulus clouds and evaluation with in situ and ground-based observations. *Journal of Geophysical Research: Atmospheres*, **120** (12), 5993–6014.
- Feingold, G., I. Koren, H. Wang, H. Xue, and W. A. Brewer, 2010: Precipitation-generated oscillations in open cellular cloud fields. *Nature*, **466** (7308), 849–852.
- Fletcher, J., S. Mason, and C. Jakob, 2016: The climatology, meteorology, and boundary layer structure of marine cold air outbreaks in both hemispheres. *Journal of Climate*, **29** (6), 1999–2014.
- Fridlind, A. M., and Coauthors, 2017: Derivation of aerosol profiles for mc3e convection studies and use in simulations of the 20 may squall line case. *Atmospheric Chemistry and Physics*, **17** (9), 5947–5972.
- Gelaro, R., and Coauthors, 2017: The modern-era retrospective analysis for research and applications, version 2 (merra-2). *Journal of climate*, **30** (14), 5419–5454.
- Ghan, S., and Coauthors, 2016: Challenges in constraining anthropogenic aerosol effects on cloud radiative forcing using present-day spatiotemporal variability. *Proceedings of the National Academy of Sciences*, **113** (21), 5804–5811.
- Glassmeier, F., F. Hoffmann, J. S. Johnson, T. Yamaguchi, K. S. Carslaw, and G. Feingold, 2021: Aerosol-cloud-climate cooling overestimated by ship-track data. *Science*, **371** (6528), 485–489.
- Hersbach, H., and Coauthors, 2020: The era5 global reanalysis. URL <https://rmets.onlinelibrary.wiley.com/doi/abs/10.1002/qj.3803>, 1999–2049 pp., <https://doi.org/https://doi.org/10.1002/qj.3803>.
- Knop, I., S. E. Bansmer, V. Hahn, and C. Voigt, 2021: Comparison of different droplet measurement techniques in the braunschweig icing wind tunnel. *Atmospheric Measurement Techniques*, **14** (2), 1761–1781.
- Lawson, R. P., D. O’Connor, P. Zmarzly, K. Weaver, B. Baker, Q. Mo, and H. Jonsson, 2006: The 2d-s (stereo) probe: Design and preliminary tests of a new airborne, high-speed, high-resolution particle imaging probe. *Journal of Atmospheric and Oceanic Technology*, **23** (11), 1462–1477.
- Lee, S. S., J. E. Penner, and S. M. Saleeby, 2009: Aerosol effects on liquid-water path of thin stratocumulus clouds. *Journal of Geophysical Research: Atmospheres*, **114** (D7).
- Li, X.-Y., and Coauthors, 2021: Large-eddy simulations of marine boundary-layer clouds associated with cold air outbreaks during the activate campaign—part 1: Case setup and sensitivities to large-scale forcings. *Journal of the Atmospheric Sciences*.
- McCoy, D. T., P. Field, H. Gordon, G. S. Elsaesser, and D. P. Grosvenor, 2020: Untangling causality in midlatitude aerosol–cloud adjustments. *Atmospheric Chemistry and Physics*, **20** (7), 4085–4103.
- Minnis, P., and Coauthors, 2008: Near-real time cloud retrievals from operational and research meteorological satellites. *Remote Sensing of Clouds and the Atmosphere XIII*, International Society for Optics and Photonics, Vol. 7107, 710703.
- Minnis, P., and Coauthors, 2021: Ceres modis cloud product retrievals for edition 4, part i: Algorithm changes. *IEEE Trans. Geosci. Remote Sens.*, **51** (4), 2744–2780, <https://doi.org/10.1109/TGRS.2020.3008866>.
- Moore, R. H., and Coauthors, 2021: Sizing response of the ultra-high sensitivity aerosol spectrometer (uhsas) and laser aerosol spectrometer (las) to changes in submicron aerosol composition and refractive index. *Atmospheric Measurement Techniques*, **14** (6), 4517–4542.
- Noble, S. R., and J. G. Hudson, 2015: Modis comparisons with north-eastern pacific in situ stratocumulus microphysics. *Journal of Geophysical Research: Atmospheres*, **120** (16), 8332–8344.
- Painemal, D., P. Minnis, J. K. Ayers, and L. O’Neill, 2012: Goes-10 microphysical retrievals in marine warm clouds: Multi-instrument validation and daytime cycle over the southeast pacific. *Journal of Geophysical Research: Atmospheres*, **117** (D19).
- Painemal, D., and P. Zuidema, 2011: Assessment of modis cloud effective radius and optical thickness retrievals over the southeast pacific with vocals-rsx in situ measurements. *Journal of Geophysical Research: Atmospheres*, **116** (D24).
- Painemal, D., and Coauthors, 2021a: Evaluation of satellite retrievals of liquid clouds from the goes-13 imager and modis over the midlatitude north atlantic during naames campaign. *Atmospheric Measurement Techniques Discussions*, 1–23.

- Painemal, D., and Coauthors, 2021b: An overview of atmospheric features over the western north atlantic ocean and north american east coast—part 2: Circulation, boundary layer, and clouds. *Journal of Geophysical Research: Atmospheres*, **126** (6), e2020JD033423.
- Petters, M., and S. Kreidenweis, 2007: A single parameter representation of hygroscopic growth and cloud condensation nucleus activity. *Atmospheric Chemistry and Physics*, **7** (8), 1961–1971.
- Rosenfeld, D., Y. Kaufman, and I. Koren, 2006: Switching cloud cover and dynamical regimes from open to closed benard cells in response to the suppression of precipitation by aerosols. *Atmospheric Chemistry and Physics*, **6** (9), 2503–2511.
- Seethala, C., and Coauthors, 2021: On assessing era5 and merra2 representations of cold-air outbreaks across the gulf stream. *Geophysical Research Letters*, **48** (19), e2021GL094364.
- Seifert, A., and K. D. Beheng, 2006: A two-moment cloud microphysics parameterization for mixed-phase clouds. part 1: Model description. *Meteorology and atmospheric physics*, **92** (1), 45–66.
- Seifert, A., T. Heus, R. Pincus, and B. Stevens, 2015: Large-eddy simulation of the transient and near-equilibrium behavior of precipitating shallow convection. *Journal of Advances in Modeling Earth Systems*, **7** (4), 1918–1937.
- Seinfeld, J. H., and Coauthors, 2016: Improving our fundamental understanding of the role of aerosol–cloud interactions in the climate system. *Proceedings of the National Academy of Sciences*, **113** (21), 5781–5790.
- Sorooshian, A., and Coauthors, 2019: Aerosol–cloud–meteorology interaction airborne field investigations: Using lessons learned from the us west coast in the design of activate off the us east coast. *Bulletin of the American Meteorological Society*, **100** (8), 1511–1528.
- Sorooshian, A., and Coauthors, 2020: Atmospheric research over the western north atlantic ocean region and north american east coast: a review of past work and challenges ahead. *Journal of Geophysical Research: Atmospheres*, **125** (6), e2019JD031626.
- Stevens, B., and G. Feingold, 2009: Untangling aerosol effects on clouds and precipitation in a buffered system. *Nature*, **461** (7264), 607–613.
- Tornow, F., A. S. Ackerman, and A. M. Fridlind, 2021: Preconditioning of overcast-to-broken cloud transitions by riming in marine cold air outbreaks. *Atmospheric Chemistry and Physics Discussions*, 1–25.
- Trepte, Q. Z., and Coauthors, 2019: Global cloud detection for ceres edition 4 using terra and aqua modis data. *IEEE Transactions on Geoscience and Remote Sensing*, **57** (11), 9410–9449.
- Twomey, S., 1977: The influence of pollution on the shortwave albedo of clouds. *Journal of the atmospheric sciences*, **34** (7), 1149–1152.
- Voigt, C., and Coauthors, 2010: In-situ observations of young contrails—overview and selected results from the concert campaign. *Atmospheric chemistry and physics*, **10** (18), 9039–9056.
- Wang, H., and G. Feingold, 2009a: Modeling mesoscale cellular structures and drizzle in marine stratocumulus. part i: Impact of drizzle on the formation and evolution of open cells. *Journal of the Atmospheric Sciences*, **66** (11), 3237–3256.
- Wang, H., and G. Feingold, 2009b: Modeling mesoscale cellular structures and drizzle in marine stratocumulus. part ii: The microphysics and dynamics of the boundary region between open and closed cells. *Journal of the atmospheric sciences*, **66** (11), 3257–3275.
- Zhang, Z., X. Dong, B. Xi, H. Song, P.-L. Ma, S. J. Ghan, S. Platnick, and P. Minnis, 2017: Intercomparisons of marine boundary layer cloud properties from the arm cap-mbl campaign and two modis cloud products. *Journal of Geophysical Research: Atmospheres*, **122** (4), 2351–2365.